

Plio–Pleistocene climate sensitivity evaluated using high–resolution CO₂ records

M. A. Martínez-Botí^{1*}, G. L. Foster^{1*}, T. B. Chalk¹, E. J. Rohling^{1,2}, P. F. Sexton³, D. J. Lunt^{4,5}, R. D. Pancost^{5,6}, M. P. S. Badger^{5,6} & D. N. Schmidt^{5,7}

Theory and climate modelling suggest that the sensitivity of Earth's climate to changes in radiative forcing could depend on the background climate. However, palaeoclimate data have thus far been insufficient to provide a conclusive test of this prediction. Here we present atmospheric carbon dioxide (CO₂) reconstructions based on multi-site boron-isotope records from the late Pliocene epoch (3.3 to 2.3 million years ago). We find that Earth's climate sensitivity to CO₂-based radiative forcing (Earth system sensitivity) was half as strong during the warm Pliocene as during the cold late Pleistocene epoch (0.8 to 0.01 million years ago). We attribute this difference to the radiative impacts of continental ice-volume changes (the ice–albedo feedback) during the late Pleistocene, because equilibrium climate sensitivity is identical for the two intervals when we account for such impacts using sea-level reconstructions. We conclude that, on a global scale, no unexpected climate feedbacks operated during the warm Pliocene, and that predictions of equilibrium climate sensitivity (excluding long-term ice–albedo feedbacks) for our Pliocene-like future (with CO₂ levels up to maximum Pliocene levels of 450 parts per million) are well described by the currently accepted range of an increase of 1.5 K to 4.5 K per doubling of CO₂.

Since the start of the industrial revolution, the concentration of atmospheric CO₂ (and other greenhouse gases) has increased dramatically (from ~280 to ~400 parts per million)¹. It has been known for over 100 years that changes in greenhouse gas concentration will cause the surface temperature of Earth to vary². A wide range of observations reveals that the sensitivity of Earth's surface temperature to radiative forcing amounts to ~3 K warming per doubling of atmospheric CO₂ concentration (with a 66% confidence range of 1.5–4.5 K; see refs 1 and 3), caused by direct radiative forcing by CO₂ plus the action of a number of fast-acting positive feedback mechanisms, mainly related to atmospheric water vapour content and sea-ice and cloud albedo. Uncertainty in the magnitude of these feedbacks confounds our ability to determine the exact equilibrium climate sensitivity (ECS; the equilibrium global temperature change for a doubling of CO₂ on timescales of about a century, after all 'fast' feedbacks have had time to operate; see ref. 3 for more detail). Although the likely range of values for ECS is 1.5–4.5 K per CO₂ doubling, there is a small but finite possibility that climate sensitivity may exceed 5 K (see ref. 1). Understanding the likely value of ECS clearly has important implications for the magnitude, eventual impact and potential mitigation of future climate change.

Any long-range forecast of global temperature (that is, beyond the next 100 years) must also consider the possibility that ECS could depend on the background state of the climate^{4,5}. That is, in a warmer world, some feedbacks that determine ECS could become more efficient and/or new feedbacks could become active to give additional warmth for a given change in radiative forcing (such as those relating to methane cycling⁶, atmospheric water vapour concentrations^{5,7,8}, in addition to changes in the relative opacity of CO₂ to long-wave radiation^{5,9}). One approach to identify whether ECS depends on the climate background state is to

reconstruct ECS during periods in the geological past when Earth was warmer than today.

The Pliocene (2.6–5.3 million years (Myr) ago) is one such time, with the warmest intervals between 3.0 Myr and 3.3 Myr ago about 3 K globally warmer than pre-industrial times^{10,11}; the mean sea level was 12–32 m above the present level^{12,13}. Although most of this warmth is commonly ascribed to increased atmospheric CO₂ levels¹⁴, it has been suggested that simple comparisons of the observed temperature change in the geological record with the climate forcing from CO₂ alone are unable to constrain ECS¹⁰. Instead, a parameter termed the Earth system sensitivity (ESS) is defined, as the change in global temperature for a doubling of CO₂ once both fast and slow feedbacks have acted and the whole Earth system has reached equilibrium. (In contrast, ECS excludes the slow feedbacks; for a discussion of fast versus slow feedbacks, see ref. 3.) The most important slow feedbacks are those related to ice-albedo and vegetation-albedo changes. Because of these slow feedbacks, Pliocene ESS is thought to have been ~50% higher than ECS^{10,15}, with some existing geological data suggesting a Pliocene ESS range of 7–10 K per CO₂ doubling¹⁶, which greatly exceeds a modern ESS estimate of ~4 K per CO₂ doubling¹⁰. If ECS was similarly enhanced, then that would imply that either extra positive fast feedbacks operated, or that existing positive fast feedbacks were more efficient, thus increasing the temperature response for a given level of CO₂ forcing.

Understanding past climate sensitivity depends critically on the accuracy of the CO₂ data used. Despite a tendency towards increased agreement between different CO₂ proxies¹⁷, individual estimates of the partial pressure of CO₂ (p_{CO_2}) for the Pliocene still range from ~190 μatm to ~440 μatm (Fig. 1a, b) and there is little coherence in the trends described by the various techniques (Fig. 1a, b). This hinders any effort to accurately

¹Ocean and Earth Science, University of Southampton, National Oceanography Centre Southampton, Southampton, SO14 3ZH, UK. ²Research School of Earth Sciences, The Australian National University, Canberra, Australian Capital Territory 2601, Australia. ³Centre for Earth, Planetary, Space and Astronomical Research, The Open University, Milton Keynes, MK7 6AA, UK. ⁴School of Geographical Sciences, University of Bristol, University Road, Bristol, BS8 1SS, UK. ⁵The Cabot Institute, University of Bristol, Bristol BS8 1UJ, UK. ⁶Organic Geochemistry Unit, School of Chemistry, University of Bristol, Bristol BS8 1TS, UK. ⁷School of Earth Sciences, University of Bristol, Wills Memorial Building, Bristol, BS8 1RJ, UK.

*These authors contributed equally to this work.

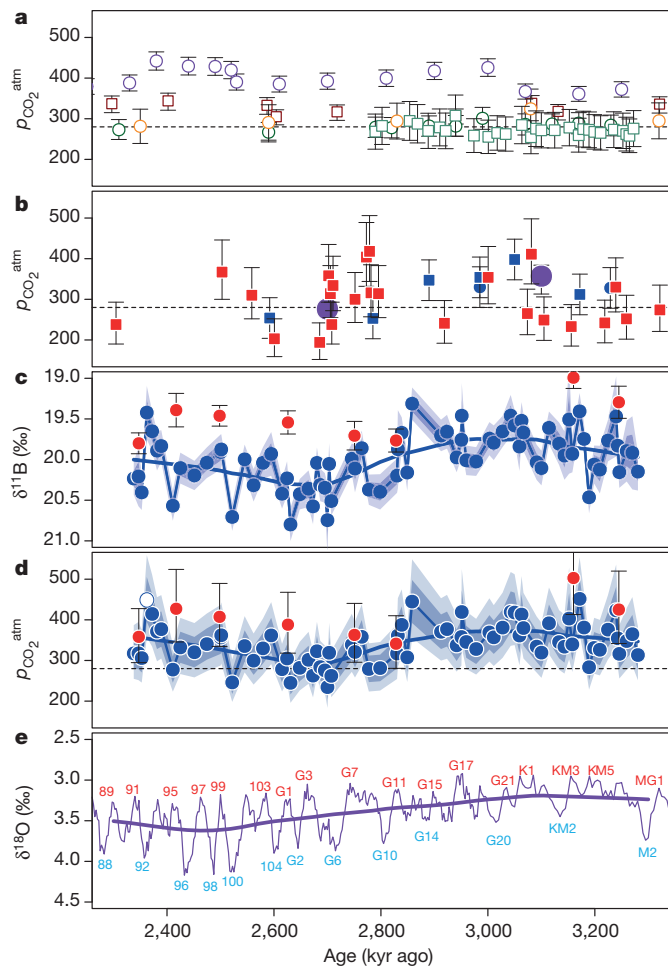


Figure 1 | Records of late Pliocene/early Pleistocene $p_{\text{CO}_2}^{\text{atm}}$. **a**, $p_{\text{CO}_2}^{\text{atm}}$ based on $\delta^{13}\text{C}$ of sedimentary alkenones (dark green circles (ODP 999)²⁵; aquamarine squares (ODP 999)²⁶; dark orange (ODP 1208)¹⁶; purple circles (ODP 806)¹⁶; and dark red squares (ODP 925)⁴⁹). Error bars are uncertainty in $p_{\text{CO}_2}^{\text{atm}}$ at the 95% level of confidence. **b**, $\delta^{11}\text{B}$ of planktic foraminifera from ODP 999 (blue circles for *Globigerinoides sacculifer*²⁵ and blue squares for *G. ruber*²⁵; red squares for *G. sacculifer*²³) and stomatal density of fossil leaves (purple filled circle)⁵⁰. Error bars are uncertainty in $p_{\text{CO}_2}^{\text{atm}}$ at the 95% level of confidence. **c**, New boron isotope data (this study) from ODP 999 (blue circles) and ODP 662 (red circles). Error bands for ODP 999 denote 1 standard deviation (sd) (dark blue) and 2 sd (light blue) analytical uncertainty; error bars for ODP 662 show 2 sd analytical uncertainty. **d**, Atmospheric p_{CO_2} determined from data shown in **c** for ODP 999 (blue circles) and ODP 662 (red circles). Error band encompasses 68% (dark blue) and 95% (light blue) of 10,000 Monte Carlo simulations of $p_{\text{CO}_2}^{\text{atm}}$ using the data in **c** and a full propagation of all the key uncertainties (see Methods). For ODP 662 error bars encompass 95% of 10,000 simulations. Dotted lines show the modelled threshold of Northern Hemisphere glaciation (280 μatm)³³. **e**, Benthic $\delta^{18}\text{O}$ stack²², with prominent marine isotope stages labelled (blue for glacial, red for interglacial stages). Thick lines on several panels are non-parametric smoothers through the data. The blue open circle in **d** highlights the data point that is identified as an outlier in Fig. 2 and not used in subsequent regressions.

constrain Pliocene ECS or ESS. To better determine Pliocene CO_2 levels, we generated a new record, based on the boron isotopic composition ($\delta^{11}\text{B}$) of the surface mixed-layer dwelling planktic foraminiferal species *Globigerinoides ruber* from Ocean Drilling Program (ODP) Site 999 (Caribbean Sea, $12^\circ 44.64' \text{N}$, $78^\circ 44.36' \text{W}$, 2,838 m water depth; Extended Data Fig. 1) at a temporal resolution (one sample about every 13,000 years (13 kyr); Fig. 1c) that is more than three times higher than previous $\delta^{11}\text{B}$ records (one sample every 50 kyr; Fig. 1b). The $\delta^{11}\text{B}$ of *G. ruber* is a well-constrained function of pH (ref. 18) and seawater pH is well correlated with $[\text{CO}_2]_{\text{aq}}$ (the aqueous concentration of CO_2),

because both are a function of the ratio of alkalinity to total dissolved carbon in seawater. In the absence of major changes in surface hydrography, $[\text{CO}_2]_{\text{aq}}$ is largely a function of atmospheric CO_2 levels, and $\delta^{11}\text{B}$ -derived CO_2 has been demonstrated to be an accurate recorder of atmospheric CO_2 (Extended Data Fig. 2a)^{18–20}. Today, the surface water at ODP Site 999 is close to equilibrium with the atmosphere with respect to CO_2 (expressed here as $\Delta p_{\text{CO}_2} = p_{\text{CO}_2}^{\text{sw}} - p_{\text{CO}_2}^{\text{atm}} = +21 \mu\text{atm}$; Extended Data Fig. 1)^{18,21} and has remained so for at least the past 130 kyr (Extended Data Fig. 2)¹⁸. ODP Site 999 also benefits from a detailed astronomically calibrated age model²² and high abundance of well-preserved planktic foraminifera throughout the past 4 Myr (refs 23, 24). During our study interval it is also unlikely to have been influenced by long-term oceanographic changes such as the emergence of the Panama isthmus ~ 3.5 Myr ago (see detailed discussion in ref. 23). To increase confidence that atmospheric CO_2 changes are driving our pH (and hence our $p_{\text{CO}_2}^{\text{sw}}$) record for ODP Site 999 and that the air–sea CO_2 disequilibrium remained similar to modern values, we also present lower-resolution $\delta^{11}\text{B}$ data from *G. ruber* from ODP Site 662 (equatorial Atlantic, Fig. 1c; $1^\circ 23.41' \text{S}$, $11^\circ 44.35' \text{W}$, 3,821 m water depth; Extended Data Fig. 1), where current mean annual Δp_{CO_2} is $+29 \mu\text{atm}$ with a seasonal maximum of $+41 \mu\text{atm}$ (ref. 21). Analytical methodology and information detailing precisely how $p_{\text{CO}_2}^{\text{sw}}$ is calculated, with full propagation of uncertainties, can be found in the Methods (with full $\delta^{11}\text{B}$ and p_{CO_2} values listed in Supplementary Tables 1 and 2).

A new record of Pliocene p_{CO_2} change

Where our data for both sites overlap in time, reconstructed $p_{\text{CO}_2}^{\text{atm}}$ values 2.3–3.3 Myr ago agree within uncertainty (Fig. 1d; Extended Data Fig. 3), and are consistent with most independent records (see Fig. 1a, b; Extended Data Fig. 2b, c), confirming that the variations we observe are predominantly driven by changes in atmospheric CO_2 concentrations. However, the enhanced resolution of our $\delta^{11}\text{B}$ - $p_{\text{CO}_2}^{\text{atm}}$ record (Fig. 1d) also reveals a hitherto undocumented^{16,23,25,26} level of structure in the CO_2 variability during the one-million-year period investigated, including a transition centred on 2.8 Myr ago, spanning ~ 200 kyr, during which average $p_{\text{CO}_2}^{\text{atm}}$ undergoes a decrease of $\sim 65 \mu\text{atm}$ (Fig. 1d).

Detailed atmospheric CO_2 measurements from ice cores show orbital-scale (~ 100 kyr) oscillations in $p_{\text{CO}_2}^{\text{atm}}$ with a peak-to-trough variation of ~ 80 – $100 \mu\text{atm}$ through the late Pleistocene (90% of the p_{CO_2} values lie between $+36 \mu\text{atm}$ and $-41 \mu\text{atm}$ of the long-term mean; Extended Data Figs 2 and 4)^{27–29}. Once the long-term trend is removed from our Plio–Pleistocene data (thick blue line in Fig. 1d), and we have taken into account our larger analytical uncertainty (see Methods), we observe orbital-scale variations in our $\delta^{11}\text{B}$ - $p_{\text{CO}_2}^{\text{atm}}$ record of only slightly smaller amplitude than the ice-core $p_{\text{CO}_2}^{\text{atm}}$ record (0–0.8 Myr) and for the last 2 Myr in other $\delta^{11}\text{B}$ -based records^{19,20,30} (Extended Data Fig. 4 and Methods), which is in clear contrast with the benthic $\delta^{18}\text{O}$, which shows increasing variability over the last 3 Myr (Fig. 1e and Extended Data Fig. 4).

Given the different amplitudes of climate variability, the observed similarity between Pliocene and late Pleistocene $p_{\text{CO}_2}^{\text{atm}}$ variability seems counter-intuitive given the notion that CO_2 is a key factor in amplifying glacial–interglacial climate change^{27–29,31,32}. This is illustrated by a well-defined nonlinear relationship in a cross plot between deep-sea benthic $\delta^{18}\text{O}$ and $\ln(\text{CO}_2/C_0)$ (where C_0 is the pre-industrial CO_2 level of 278 μatm), which accounts for the logarithmic nature of the climate forcing by CO_2 (Fig. 2b). Note also the clear overlap between Pleistocene (0–2.2 Myr) ice-core CO_2 measurements and $\delta^{11}\text{B}$ -based CO_2 reconstructions in this plot (Fig. 2b; Extended Data Fig. 2). A similar relationship is also evident in raw $\delta^{11}\text{B}$ -space (Fig. 2a). Below an inflection at about $p_{\text{CO}_2}^{\text{atm}} = 275 \pm 15 \mu\text{atm}$ (equating to $\ln(\text{CO}_2/C_0) \approx 0$), benthic $\delta^{18}\text{O}$ shows a steeper relationship with CO_2 -based forcing than it does above this value (Fig. 2). This probably reflects some combination of: (1) growth of larger Northern Hemisphere ice sheets at $p_{\text{CO}_2}^{\text{atm}}$ below $275 \pm 15 \mu\text{atm}$ (ref. 33), increasing radiative ice-albedo feedback and amplifying climate forcing by CO_2 change; (2) an increase in oxygen isotope fractionation in precipitation with increasing size of the

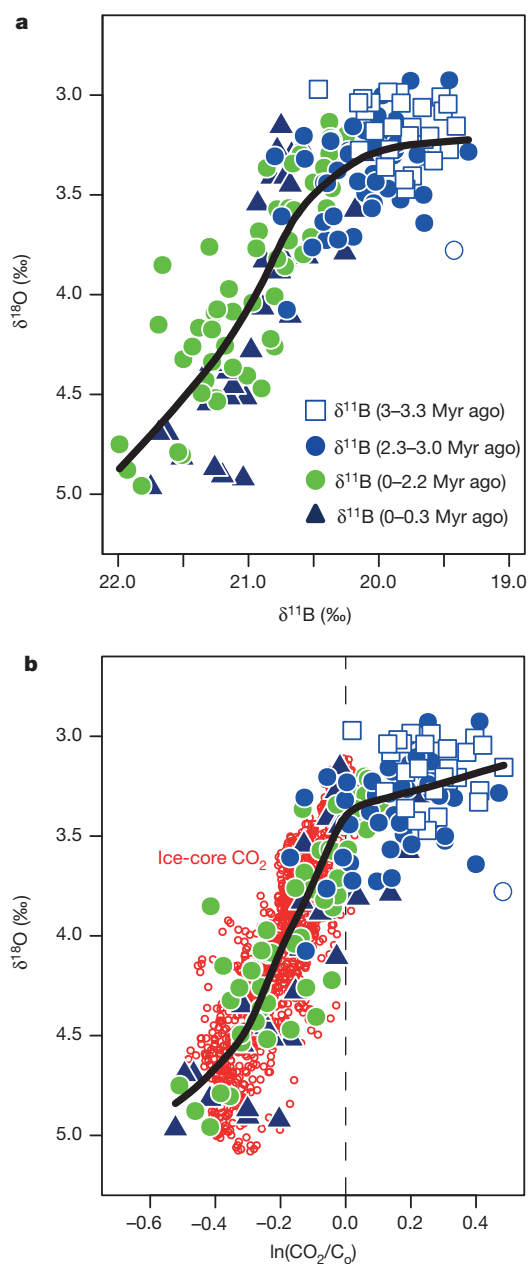


Figure 2 | Relationship between $\delta^{11}\text{B}$, climate forcing from CO_2 and $\delta^{18}\text{O}$. **a, b**, $\delta^{11}\text{B}$ versus $\delta^{18}\text{O}$ (**a**) and $\ln(\text{CO}_2/C_0)$ versus $\delta^{18}\text{O}$ (**b**) for data from the last 3 Myr. Boron data in **a** are from this study (blue open and closed circles) and published studies (green circles³⁰; blue triangles²⁰). Ice-core CO_2 data are shown as open red circles^{27–29}. The vertical dashed line is at a CO_2 of 278 μatm . The data point removed from subsequent regression analysis is shown as open blue circles in **a** and **b**. Note that for clarity the $\delta^{11}\text{B}$ – p_{CO_2} data from ref. 23 are not plotted. The black line is a non-parametric regression through all the data shown. The $\delta^{11}\text{B}$ data from ref. 30 have been corrected for laboratory and inter-species differences through a comparison between core-top $\delta^{11}\text{B}$ values.

ice sheets, which leads to a proportionally greater ^{18}O enrichment in seawater³⁴; and (3) potentially stronger deep-sea cooling at low $p_{\text{CO}_2}^{\text{atm}}$ due to the high-latitude-focused influences of the ice-albedo feedback process. These findings highlight the profound impacts of Northern Hemisphere ice-sheet growth on climate variability in the Pleistocene^{31,32}, relative to the Pliocene (Fig. 2b).

Our data show that the $\sim 275 \pm 15 \mu\text{atm}$ threshold was first crossed ~ 2.8 Myr ago during Marine Isotope Stage (MIS) G10 (Fig. 1d, horizontal dashed line), and—more persistently—during subsequent MISs G6 (2.72 Myr ago), G2 (2.65 Myr ago), and 100 (2.52 Myr ago), when values

as low as $233 \pm_{53}^{63} \mu\text{atm}$ (95% confidence) were reached and when intervening interglacial values also seem to have been suppressed (Fig. 1c, d). These isotope stages are notable in that they are associated with an increase in the amplitude of glacial–interglacial sea-level oscillations (Extended Data Fig. 5b)^{12,13,35} and coincide with the timing of the first substantial continental glaciations of Europe, North America and the Canadian Cordillera, as reconstructed by ice-rafted debris and observations of relic continental glacial deposits^{36–38}. Hence, our high-resolution $p_{\text{CO}_2}^{\text{atm}}$ record robustly confirms previous hypotheses^{16,23,25,39} (based on low-resolution CO_2 data) that the first substantial stages of glaciation in the Northern Hemisphere, as well as a recently recognized deep-sea cooling during the late Pliocene/early Pleistocene¹³, coincided with a significant decline in mean atmospheric $p_{\text{CO}_2}^{\text{atm}}$ 2.7–2.9 Myr ago of ~ 40 – $90 \mu\text{atm}$ (the mean value of $p_{\text{CO}_2}^{\text{atm}}$ 3.0–3.2 Myr ago minus its mean 2.4–2.7 Myr ago = $66 \pm 26 \mu\text{atm}$; two-tailed $P < 0.001$, $n = 40$).

Efficiency of climate feedbacks

The high fidelity of the boron isotope $\text{pH}/p_{\text{CO}_2}^{\text{atm}}$ proxy (Extended Data Fig. 2), coupled with the high resolution of our $p_{\text{CO}_2}^{\text{atm}}$ record, offers an opportunity to examine the sensitivity of Earth’s climate system to forcing by CO_2 during a period when Earth’s climate was, on average, warmer than today⁴⁰. For this exercise, global temperature estimates are also needed. We consider two approaches for this. The first is an estimate of global mean annual surface air temperature change (ΔMAT) over the last 3.5 Myr, from a scaling of the Northern Hemisphere climate required to drive an ice-sheet model to produce deep-ocean temperature and ice-volume changes consistent with benthic $\delta^{18}\text{O}$ data (Fig. 3a, b)³⁵. This approach produces a continuous record of global temperature that agrees well with independent constraints for discrete time intervals (see ref. 35).

We supplement ΔMAT with a record from a second approach, which is independent from benthic $\delta^{18}\text{O}$ values. For this, we generated a sea surface temperature stack (SST_{st}) from 0 to 3.5 Myr ago (Fig. 3c, d), comprising ten high-resolution (average ~ 4 kyr) SST records based on alkenone unsaturation ratios (expressed as the U_{37}^K palaeotemperature index), from latitudes between 41°S and 57°N . The selected sites (see Extended Data Fig. 1b) all offer near-continuous temporal coverage of the last 3.5 Myr (see Methods). Our SST stack agrees well with independent, higher-density compilations of global SST change^{32,41} (blue line in Fig. 3c), indicating that SST_{st} offers a reliable approximation of global SST change (see Methods for more details). Moreover, our SST stack allows us to directly compare the major SST changes, within the same archives, between the Plio-Pleistocene and late Pleistocene.

When comparing temperature records from the two approaches considered, it must be emphasized that ΔMAT reflects the global mean annual surface air temperature change, while the SST stack approximates the global mean sea surface temperature change. Hence, their amplitudes of variability will be different, mainly because SST_{st} does not include temperature changes over land. Approximately, $\Delta\text{SST} = \Delta\text{MAT} \times 0.66$ (refs 32 and 42), but a direct conversion is not needed here, because we merely aim to contrast Pliocene climate behaviour with that for the Pleistocene, within the same data types.

To determine the sensitivity of global SST and ΔMAT to CO_2 forcing in the Pliocene and Pleistocene, we use a time series of forcing calculated from our new and existing CO_2 records (Fig. 3e–h), and regress these against both ΔMAT and the SST stack (Fig. 3a to d; Supplementary Tables 1–3). The regression slopes then describe the average temperature change ΔT (in units of K) per watt per square metre of forcing (ΔF) for each time interval. These gradients therefore approximate the commonly used sensitivity parameter $S = \Delta T/\Delta F$ (in units of $\text{K W}^{-1} \text{m}^2$) for describing global temperature change for a given forcing³. In this scheme, a doubling of atmospheric CO_2 is equivalent to a forcing of 3.7 W m^{-2} , so that for the 66% confidence interval of modern climate sensitivity quoted by ref. 1, the present-day equilibrium value of S (which we denote S^a , where superscript ‘a’ is for ‘actuo’, after ref. 3) is $1.5/3.7$ to $4.5/3.7 = 0.4$ – $1.2 \text{ K W}^{-1} \text{m}^2$. However, using palaeoclimate

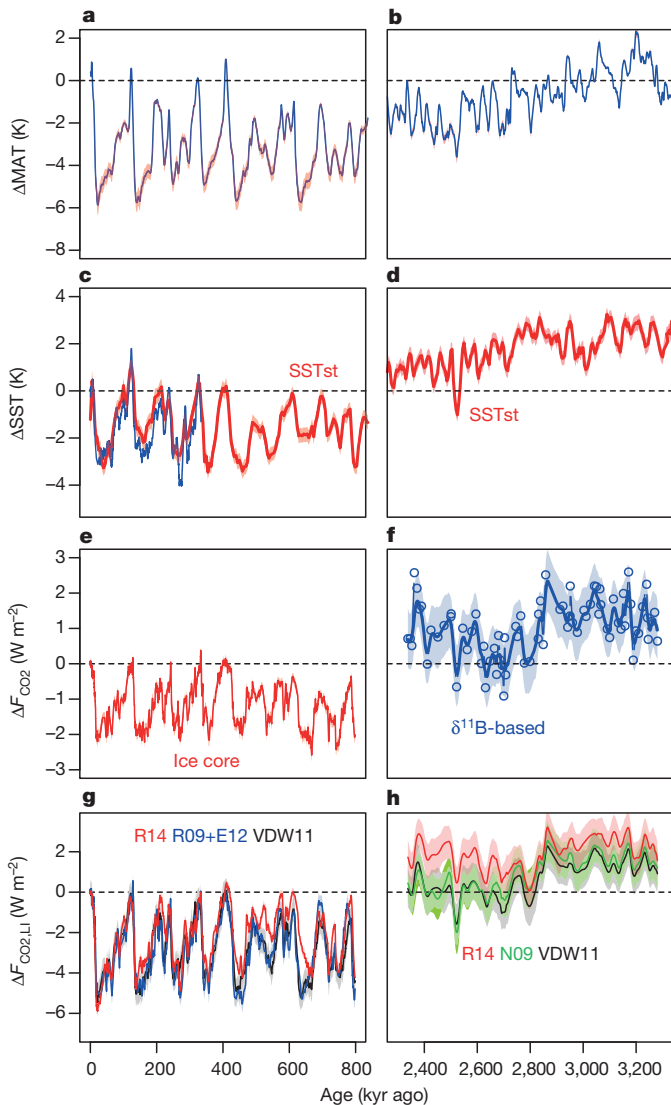


Figure 3 | Pleistocene and late Pliocene time series. **a, b**, ΔMAT^{35} . **c, d**, ΔSST . Data from this study are shown in red and from a stack of a more comprehensive compilation³² in blue. Uncertainty envelopes at 95% confidence for both temperature records are shown in red. **e**, ΔF_{CO_2} for the Pleistocene from ice-core data^{27–29}. **f**, ΔF_{CO_2} for the late Pliocene, calculated using the CO_2 data from this study. **g**, $\Delta F_{\text{CO}_2, \text{LI}}$ calculated using data in **e** and published sea-level records (R14 from ref. 13, VDW11 from ref. 35 and R09+E12 from ref. 44 for 0–520 kyr and ref. 45 for 520–800 kyr). **h**, $\Delta F_{\text{CO}_2, \text{LI}}$ for the late Pliocene calculated using the CO_2 data from this study and published sea-level records (N09 from ref. 46 recalculated by ref. 12, R14 from ref. 13, VDW11 from ref. 35). Error bands in **e** to **h** represent the uncertainty in smoothed CO_2 record and sea level (at 95% confidence), propagated using a Monte Carlo approach ($n = 1,000$) for each reconstruction.

data it is not possible to determine the direct equivalent of S^a ; instead, such studies constrain a ‘past’ parameter (S^p), which includes the combined action of both fast and slow feedbacks³. Note that ESS (in units of K) = $S^p \times 3.7$. Explicitly accounting for slow feedback processes in determinations of S^p can make it approximate S^a (ref. 3). Following ref. 3, an S^p estimate after accounting for carbon-cycle feedback is indicated by S_{CO_2} , and one accounting for both carbon-cycle feedbacks and feedbacks between land-ice and albedo feedbacks is $S_{\text{CO}_2, \text{LI}}$, where the latter gives a useful approximation of S^a . We follow this approach, using $S^p = \Delta\text{MAT}/\Delta F$ and $S^{p, \text{SST}} = \Delta\text{SST}/\Delta F$ (both in units of $\text{K W}^{-1} \text{m}^2$). Note that our determinations of the sensitivity parameter are based on our entire reconstructed time series, rather than on a simple comparison between a limited Pliocene average and the modern average, as was

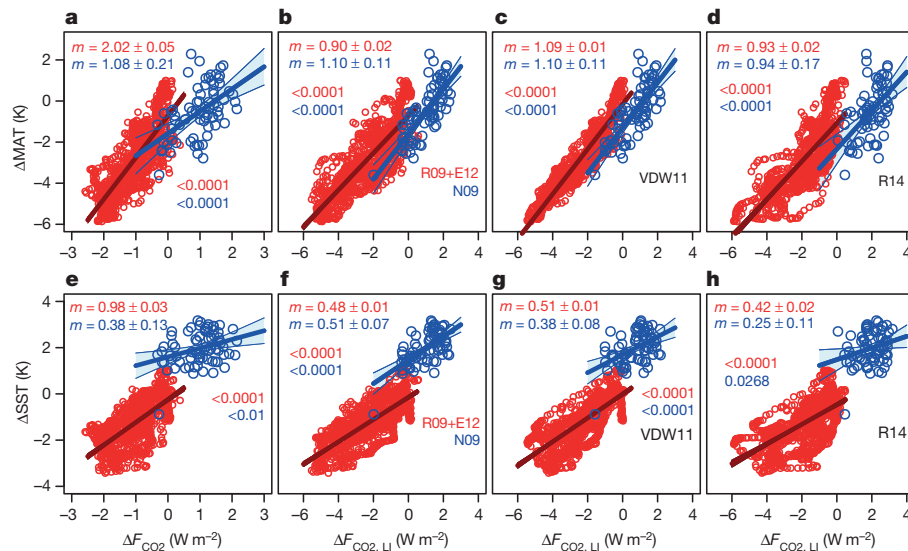
done in previous studies^{3,16}. Since we calculate a S^p (and $S^{p, \text{SST}}$) for the Pliocene and compare this to the late Pleistocene S^p (and $S^{p, \text{SST}}$), we also avoid complications caused by independent changes in boundary conditions (such as topographic changes)³⁹ because we assess sensitivity within each relatively short time window (2.3–3.3 Myr ago versus 0–0.8 Myr ago). In addition, our approach emphasizes relative changes in CO_2 levels and temperature over the intervals considered, rather than absolute values. This improves accuracy because relative changes are much better constrained than absolute temperature and $p_{\text{CO}_2}^{\text{atm}}$ values from proxy data (see Methods for further discussion).

Preliminary regression of ΔMAT against Pliocene $p_{\text{CO}_2}^{\text{atm}}$ identified one data point (at 2,362 kyr; white circle in Figs 1d and 2) with a particularly large residual and notable leverage on the least-squares regression (a high Cook’s distance). With interglacial-like $p_{\text{CO}_2}^{\text{atm}}$ values but glacial-like $\delta^{18}\text{O}$ values (Fig. 2), this point may reflect a chronological error, or a short period of unusually high air–sea disequilibrium with respect to CO_2 at ODP Site 999. To avoid the influence of this one point on subsequent linear regressions, we have removed it from our $\delta^{11}\text{B}$ – $p_{\text{CO}_2}^{\text{atm}}$ record. The remaining $p_{\text{CO}_2}^{\text{atm}}$ data (73 points) were interpolated to a constant resolution (1 kyr), smoothed with a 20-kyr moving average to reduce short-term noise and resampled back to the original data spacing (about one sample every 13 kyr). A Monte Carlo approach was followed to determine uncertainties for this smoothed record given the uncertainty in the $\delta^{11}\text{B}$ -derived $p_{\text{CO}_2}^{\text{atm}}$. Radiative forcing changes due to $p_{\text{CO}_2}^{\text{atm}}$ changes are calculated using $\Delta F_{\text{CO}_2} = 5.35 \ln(\text{CO}_2/C_0)$, where $C_0 = 278 \mu\text{atm}$ (Fig. 3)⁴³. We ignore mean annual forcing by orbital variations because it is small ($<0.5 \text{ W m}^{-2}$ with a periodicity of 100–400 kyr)^{31,32} and averages out over the length of our records. Linear regressions of ΔMAT and SST_{st} versus ΔF_{CO_2} were performed using an approach that yields a probabilistic estimate of slope, and hence sensitivity to CO_2 forcing ($S_{\text{CO}_2} = \Delta T/\Delta F_{\text{CO}_2}$ or $S_{\text{CO}_2, \text{LI}} = \Delta T/\Delta F_{\text{CO}_2, \text{LI}}$), which fully accounts for uncertainties in both x and y variables (see Methods and Fig. 4). Figure 5a–d displays probability density functions of the determinations of slope for each time interval. This analysis reveals that, irrespective of the global temperature record used (ΔMAT or the SST_{st}), the average global sensitivity of Earth’s climate to forcing by CO_2 only (S_{CO_2}) is approximately twice as high for the Pleistocene as it is for the Pliocene (Figs 4 and 5). This validates previous inferences of a strong additional feedback factor during the Pleistocene (at $p_{\text{CO}_2}^{\text{atm}}$ levels below $\sim 280 \mu\text{atm}$), which probably arises from the growth and retreat of large Northern Hemisphere ice sheets and their role in changing global albedo^{31,32}.

Given that, to a first order, the Earth system responds to radiative forcing in a consistent fashion, largely independent of the nature of that forcing⁸, we can determine the climate forcing arising from continental ice albedo changes via a relatively simple parameterization of sea-level change ($\Delta F_{\text{LI}} = \text{sea-level change (in units of metres)} \times 0.0308 \text{ W m}^{-2}$; following refs 31 and 32). Several reconstructions of sea-level change partially or completely span the last 3.5 Myr (for example, refs 13, 35, 44, 45 and 46 recalculated by ref. 12), and we explore the implications of each of these independent records. Cross-plots of combined CO_2 and ice-albedo forcing ($\Delta F_{\text{CO}_2} + \Delta F_{\text{LI}} = \Delta F_{\text{CO}_2, \text{LI}}$) versus ΔMAT and SST_{st} are shown in Fig. 4 for the Pliocene and Pleistocene. Figure 5e–h displays the influence of choices of temperature and sea-level record on our determinations of $S_{\text{CO}_2, \text{LI}} (= \Delta T/\Delta F_{\text{CO}_2, \text{LI}})$. In contrast to S_{CO_2} , $S_{\text{CO}_2, \text{LI}}$ is similar for both the Pliocene and Pleistocene, regardless of temperature record or other parameter choices (Fig. 5). This robustly indicates that the apparent difference between Pliocene and Pleistocene climate sensitivity arises almost entirely from ice-albedo feedback influences.

It also implies that all of the other feedbacks that amplify climate forcing by CO_2 (for example, sea-ice and cloud albedo, water vapour, vegetation, aerosols, other greenhouse gases) must have operated with similar efficiencies during both the Pliocene and Pleistocene. Thus, we find no evidence that additional (unexpected) positive feedbacks had become active to amplify Earth system sensitivity to CO_2 forcing during the warm Pliocene. Alternatively, if additional positive feedbacks did become active

Figure 4 | Cross plots of forcing and temperature response. **a**, ΔMAT versus ΔF_{CO_2} , and **b–d**, ΔMAT versus $\Delta F_{\text{CO}_2, \text{LI}}$, for the following sea-level records detailed in the caption for Fig. 3: **b**, R09+E12^{44,45} and N09^{12,46}; **c**, VDW11³⁵; and **d**, R14¹³. **e**, ΔSST versus ΔF_{CO_2} and **f–h**, ΔSST versus $\Delta F_{\text{CO}_2, \text{LI}}$ for the same sea-level records as in **b–d**. In all panels, late Pleistocene data (0–800 kyr) are shown as red open circles and late Plio-Pleistocene (2,300–3,300 kyr) as blue open circles. Regression lines fitted by least-squares regression are also shown in the appropriate colour (shaded bands represent 95% confidence intervals). For **a–d** the temperature record is that of ref. 35 and for **e–h** it is the SST stack from this study. In all cases the slope m and standard error uncertainty are determined by least-squares regression. Also shown are the P values for the regressions.



(for example, an increase in steady-state methane concentration or changes in cloud properties), then their effect must have been negated by the loss of other amplifying feedbacks (for example, Arctic sea-ice) or the addition of more negative feedbacks. This finding is at odds with previous studies (such as refs 16,47), most probably because of differences in our approach to determine Pliocene climate sensitivity (that is, we determine a sensitivity within the Pliocene) and shortcomings in the proxy systems used by the earlier investigations, both in terms of CO_2 and temperatures (see ref. 48). For instance, Fig. 1d (and Extended Data Fig. 2) indicate that both orbital-scale variability in $p_{\text{CO}_2}^{\text{atm}}$ and the major decline at 2.7–2.9 Myr ago are absent from the previously used¹⁶ alkenone-based $p_{\text{CO}_2}^{\text{atm}}$ records and as a result regressions of temperature and alkenone-derived forcing are poorly defined (Extended Data Fig. 2d–f).

Constraints on climate sensitivity

Using the geological record to estimate ECS directly (and thus S^{cl}) is problematic because information on the appropriate magnitude of a number of key feedbacks (such as vegetation albedo) is typically unavailable³. Nonetheless, considerable effort has determined that ECS estimates based on the last glacial maximum fall within the range of ECS estimates from other approaches (1.5–4.5 K per CO_2 doubling, or 0.4–1.2 $\text{K W}^{-1} \text{ m}^2$; ref. 1). Our analysis implies that a similar ECS applies to the Pliocene and early Pleistocene (2.3–3.3 Myr ago; Fig. 5; Supplementary Table 4). In addition, our estimate of Pliocene S_{CO_2} using ΔMAT lies within a range of 0.6–1.5 $\text{K W}^{-1} \text{ m}^2$ (at 95% confidence), meaning that, once all feedbacks have played out for future CO_2 doubling, ESS (= $S_{\text{CO}_2} \times 3.7$) will very probably (95% confidence) be <5.2 K and will

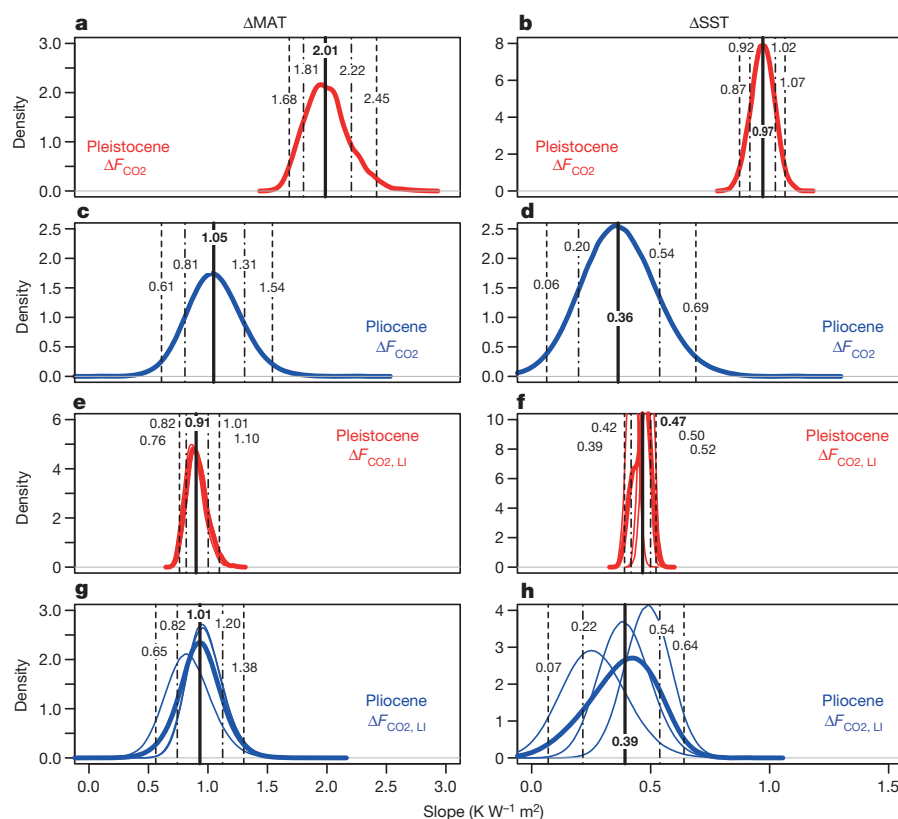


Figure 5 | Probability density functions of the slope from regressions of temperature against climate forcing. **a**, **c**, **e**, **g**, ΔMAT and **b**, **d**, **f**, **h**, ΔSST against ΔF_{CO_2} and $\Delta F_{\text{CO}_2, \text{LI}}$ for the Pleistocene (**a**, **b**, **e**, **f**) and Pliocene (**c**, **d**, **g**, **h**), taking into account the uncertainties on all variables (see text). In **e–h** individual probability density functions are shown for different choices of sea level: the combined probability density function shown in bold is the sum of these different probability density functions and therefore also incorporates uncertainty related to the choice of sea-level record. Also shown are the median (in boldface), the 68th percentile (dot-dash) and 95th percentiles (dashed).

probably (68% confidence) fall within a range of 3.0–4.4 K (Supplementary Table 4).

In May 2013, atmospheric CO₂ levels crossed the 400 parts per million threshold to values last seen during the Pliocene (Fig. 1c). Given current CO₂ emission rates, global temperatures may reach those typical of the warm periods of the Pliocene by 2050¹. Our findings suggest that, if the Earth system behaves in a similar fashion to how it did during the Pliocene as it continues to warm in the coming years, an ECS of 1.5–4.5 K per CO₂ doubling¹ probably provides a reliable description of the Earth's equilibrium temperature response to climate forcing, at least for global temperature rise up to 3 K above the pre-industrial level. Studies of even warmer intervals in the deeper geological past (well before 3.3 Myr ago) are needed to determine whether any additional climate feedbacks should be expected as Earth warms even further into the twenty-second century if CO₂ emissions continue unabated.

Online Content Methods, along with any additional Extended Data display items and Source Data, are available in the online version of the paper; references unique to these sections appear only in the online paper.

Received 1 July; accepted 5 December 2014.

- IPCC. *Climate Change 2013: The Physical Science Basis. Contribution of Working Group I to the Fifth Assessment Report of the Intergovernmental Panel on Climate Change* (eds Stocker, T. F. et al.) 1–1535 (Cambridge Univ. Press, 2013).
- Arrhenius, S. On the influence of carbonic acid in the air upon the temperature of the ground. *Philos. Mag.* **41**, 237–276 (1896).
- Rohling, E. J. et al. Making sense of palaeoclimate sensitivity. *Nature* **491**, 683–691 (2012).
- Crucifix, M. Does the Last Glacial Maximum constrain climate sensitivity? *Geophys. Res. Lett.* **33**, L18701 (2006).
- Caballero, R. & Huber, M. State-dependent climate sensitivity in past warm climates and its implication for future climate projections. *Proc. Natl Acad. Sci.* **110**, 14162–14167 (2013).
- Beerling, D. J., Fox, A., Stevenson, D. S. & Valdes, P. J. Enhanced chemistry-climate feedbacks in past greenhouse worlds. *Proc. Natl Acad. Sci. USA* **108**, 9770–9775 (2011).
- Meraner, K., Mauritsen, T. & Voigt, A. Robust increase in equilibrium climate sensitivity under global warming. *Geophys. Res. Lett.* **40**, 5944–5948 (2013).
- Hansen, J. et al. Efficacy of climate forcings. *J. Geophys. Res.* **110**, <http://dx.doi.org/10.1029/2005JD005776> (2005).
- Byrne, B. & Goldblatt, C. Radiative forcing at high concentrations of well-mixed greenhouse gases. *Geophys. Res. Lett.* **41**, 152–160 (2014).
- Lunt, D. J. et al. Earth system sensitivity inferred from Pliocene modelling and data. *Nature Geosci.* **3**, 60–64 (2010).
- Haywood, A. M. & Valdes, P. J. Modelling Pliocene warmth: contribution of atmosphere, oceans and cryosphere. *Earth Planet. Sci. Lett.* **218**, 363–377 (2004).
- Miller, K. G. et al. High tide of the warm Pliocene: implications of global sea level for Antarctic deglaciation. *Geology* **40**, 407–410 (2012).
- Rohling, E. J. et al. Sea-level and deep-sea-temperature variability over the past 5.3 million years. *Nature* **508**, 477–482 (2014).
- Lunt, D. J. et al. On the causes of mid-Pliocene warmth and polar amplification. *Earth Planet. Sci. Lett.* **321–322**, 128–138 (2012).
- Haywood, A. M. et al. Large-scale features of Pliocene climate: results from the Pliocene Model Intercomparison Project. *Clim. Past* **9**, 191–209 (2013).
- Pagani, M., Liu, Z., LaRiviere, J. & Ravello, A. C. High Earth-system climate sensitivity determined from Pliocene carbon dioxide concentrations. *Nature Geosci.* **3**, 27–30 (2010).
- Beerling, D. J. & Royer, D. L. Convergent Cenozoic CO₂ history. *Nature Geosci.* **4**, 418–420 (2011).
- Henehan, M. J. et al. Calibration of the boron isotope proxy in the planktonic foraminifera *Globigerinoides ruber* for use in palaeo-CO₂ reconstruction. *Earth Planet. Sci. Lett.* **364**, 111–122 (2013).
- Hönisch, B. & Hemming, N. G. Surface ocean pH response to variations in pCO₂ through two full glacial cycles. *Earth Planet. Sci. Lett.* **236**, 305–314 (2005).
- Foster, G. L. Seawater pH, pCO₂ and [CO₃²⁻] variations in the Caribbean Sea over the last 130 kyr: a boron isotope and B/Ca study of planktic foraminifera. *Earth Planet. Sci. Lett.* **271**, 254–266 (2008).
- Takahashi, K. et al. Climatological mean and decadal change in surface ocean pCO₂ and net sea-air CO₂ flux over the global oceans. *Deep Sea Res. II* **56**, 554–577 (2009).
- Lisiecki, L. E. & Raymo, M. E. A Pliocene-Pleistocene stack of 57 globally distributed benthic δ¹⁸O records. *Paleoceanography* **20**, <http://dx.doi.org/10.1029/2004PA001071> (2005).
- Bartoli, G., Hönisch, B. & Zeebe, R. Atmospheric CO₂ decline during the Pliocene intensification of Northern Hemisphere Glaciations. *Paleoceanography* **26**, PA4213 (2012).
- Davis, C. V., Badger, M. P. S., Bown, P. R. & Schmidt, D. N. The response of calcifying plankton to climate change in the Pliocene. *Biogeosciences* **10**, 6131–6139 (2013).
- Seki, O. et al. Alkenone and boron based Plio-Pleistocene pCO₂ records. *Earth Planet. Sci. Lett.* **292**, 201–211 (2010).
- Badger, M. P. S., Schmidt, D. N., Mackensen, A. & Pancost, R. D. High resolution alkenone palaeobarometry indicates relatively stable pCO₂ during the Pliocene (3.3 to 2.8 Ma). *Phil. Trans. R. Soc. A* **373**, 20130094 (2013).
- Petit, J. R. et al. Climate and atmospheric history of the past 420,000 years from the Vostok ice core, Antarctica. *Nature* **399**, 429–436 (1999).
- Lüthi, D. et al. High-resolution carbon dioxide concentration record 650,000–800,000 years before present. *Nature* **453**, 379–382 (2008).
- Siegenthaler, U. et al. Stable carbon cycle-climate relationship during the Late Pleistocene. *Science* **310**, 1313–1317 (2005).
- Hönisch, B., Hemming, G., Archer, D., Siddall, M. & McManus, J. Atmospheric carbon dioxide concentration across the Mid-Pleistocene Transition. *Science* **324**, 1551–1554 (2009).
- Köhler, P. et al. What caused Earth's temperature variations during the last 800,000 years? Data-based evidence on radiative forcing and constraints on climate sensitivity. *Quat. Sci. Rev.* **29**, 129–145 (2010).
- Rohling, E. J., Medina-Elizalde, M., Shepherd, J. G., Siddall, M. & Stanford, J. D. Sea surface and high-latitude temperature sensitivity to radiative forcing of climate over several glacial cycles. *J. Clim.* **25**, 1635–1656 (2012).
- DeConto, R. M. et al. Thresholds for Cenozoic bipolar glaciation. *Nature* **455**, 652–656 (2008).
- Shackleton, N. Oxygen isotope analyses and Pleistocene temperatures re-assessed. *Nature* **215**, 15–17 (1967).
- van de Wal, R. S. W., de Boer, B., Lourens, L. J., Köhler, P. & Bintanja, R. Reconstruction of a continuous high-resolution CO₂ record over the past 20 million years. *Clim. Past* **7**, 1459–1469 (2011).
- Balco, G. & Rovey, C. W., II. Absolute chronology for major Pleistocene advances of the Laurentide Ice Sheet. *Geology* **38**, 795–798 (2010).
- Bailey, I. et al. An alternative suggestion for the Pliocene onset of major northern hemisphere glaciation based on geochemical provenance of North Atlantic Ocean ice-rafted debris. *Quat. Sci. Rev.* **75**, 181–194 (2013).
- Hidy, A. J., Gosse, J. C., Froese, D. G., Bond, J. D. & Rood, D. H. A latest Pliocene age for the earliest and most extensive Cordilleran Ice Sheet in northwestern Canada. *Quat. Sci. Rev.* **61**, 77–84 (2013).
- Lunt, D. J., Foster, G. L., Haywood, A. M. & Stone, E. J. Late Pliocene Greenland glaciation controlled by a decline in atmospheric CO₂ levels. *Nature* **454**, 1102–1105 (2008).
- Dowsett, H. J. et al. Assessing confidence in Pliocene sea surface temperatures to evaluate predictive models. *Nature Clim. Change* **2**, 365–371 (2012).
- Shakun, J. D. et al. Global warming preceded by increasing carbon dioxide concentrations during the last deglaciation. *Nature* **484**, 49–54 (2012).
- Williams, R. G., Goodwin, P., Ridgwell, A. & Woodworth, P. L. How warming and steric sea level rise relate to cumulative carbon emissions. *Geophys. Res. Lett.* **39**, <http://dx.doi.org/10.1029/2012GL052771> (2012).
- Myhre, G., Highwood, E. J., Shine, K. P. & Stordal, F. New estimates of radiative forcing due to well mixed greenhouse gases. *Geophys. Res. Lett.* **25**, 2715–2718 (1998).
- Rohling, E. J. et al. Antarctic temperature and global sea level closely coupled over the past five glacial cycles. *Nature Geosci.* **2**, 500–504 (2009).
- Elderfield, H. et al. Evolution of ocean temperature and ice volume through the Mid-Pleistocene climate transition. *Science* **337**, 704–709 (2012).
- Naish, T. R. & Wilson, G. S. Constraints on the amplitude of Mid-Pliocene (3.6–2.4 Ma) eustatic sea-level fluctuations from the New Zealand shallow-marine sediment record. *Phil. Trans. R. Soc. A* **367**, 169–187 (2009).
- Fedorov, A. V. et al. Patterns and mechanisms of early Pliocene warmth. *Nature* **496**, 43–49 (2013).
- O'Brien, C. L. et al. High sea surface temperatures in tropical warm pools during the Pliocene. *Nature Geosci.* **7**, 606–611 (2014).
- Zhang, Y. G., Pagani, M., Liu, Z., Bohaty, S. M. & DeConto, R. M. A 40-million-year history of atmospheric CO₂. *Phil. Trans. R. Soc. A* **371**, 20130096 (2013).
- Kürschner, W. M., van der Burgh, J., Visscher, H. & Dilcher, D. L. Oak leaves as biosensors of late Neogene and early Pleistocene paleoatmospheric CO₂ concentrations. *Mar. Micropaleontol.* **27**, 299–312 (1996).

Supplementary Information is available in the online version of the paper.

Acknowledgements This study used samples provided by the International Ocean Discovery Program (IODP). We thank A. Milton at the University of Southampton for maintaining the mass spectrometers used in this study. S. Chery and T. Garlich are acknowledged for their help with sample preparation and we thank D. Liebrand for his assistance with time series analysis. This study was funded by NERC grants NE/H006273/1 to R.D.P., G.L.F., D.J.L. and D.N.S. (which supported M.A.M.-B. and M.P.S.B.) and NE/I006346/1 to P.F.S. and G.L.F. M.A.M.-B. was also supported by the European Community through a Marie Curie Fellowship and E.J.R. was supported by 2012 Australian Laureate Fellowship FL120100050. G.L.F. also wishes to acknowledge the support of Yale University (as Visiting Flint Lecturer).

Author Contributions M.A.M.-B. and T.B.C. collected the data and G.L.F. performed all relevant calculations. P.F.S. helped with sample preparation for δ¹³C analysis and refined the age models used for ODP Sites 999 and 662. G.L.F., M.A.M.-B. and T.B.C. constructed the first draft of the manuscript and all authors contributed specialist insights that helped refine the manuscript. G.L.F., R.D.P., D.J.L. and D.N.S. conceived the study.

Author Information Reprints and permissions information is available at www.nature.com/reprints. The authors declare no competing financial interests. Readers are welcome to comment on the online version of the paper. Correspondence and requests for materials should be addressed to G.L.F. (gavin.foster@noc.soton.ac.uk).

METHODS

Sample locations. We present new data from two deep ocean sites: ODP Site 999 (Caribbean Sea, 12° 44.64' N and 78° 44.36' W) and ODP Site 662 (equatorial Atlantic, 1° 23.41' S, 11° 44.35' W). Both sites have well-constrained age models for the Pliocene and are part of the Lisiecki and Raymo benthic foraminifera $\delta^{18}\text{O}$ stack²² (hereafter LR04). Sedimentation rates are comparable between the sites ($\sim 3\text{ cm kyr}^{-1}$ at ODP 999 and $\sim 4\text{ cm kyr}^{-1}$ at ODP 662). At ODP Site 999, seventy-four samples were analysed at an average temporal resolution of around one sample every 13 kyr, targeting several glacial and interglacial maxima. ODP Site 662 was analysed at much lower resolution (8 samples in 1,000 kyr = 1 sample every 125 kyr on average), and the chosen samples were limited to peak interglacial conditions to avoid potential upwelling influences during glacial periods³¹. The extent of the modern air–sea CO_2 disequilibrium at each location is displayed in Extended Data Fig. 1a. **Analytical methodology.** Between 90 and 200 individuals of *G. ruber* ($\sim 10\ \mu\text{g}$ per shell) were picked from the 300–355- μm size fraction from ODP Sites 999 and 662. Foraminiferal samples were crushed between cleaned glass microscope slides and subsequently cleaned according to established oxidative cleaning methods^{52–54}. After cleaning, samples were dissolved in $\sim 0.15\text{ M}$ Teflon-distilled HNO_3 , centrifuged and transferred to 5 ml Teflon vials for storage. An aliquot ($\sim 20\ \mu\text{l}$; $\sim 7\%$ of the total sample) was taken for trace element analysis. Boron was separated from the dissolved samples using Amberlite IRA-743 boron-specific anion exchange resin following established procedures²⁰. Boron isotope ratios were measured on a Thermo Scientific Neptune multicollector inductively coupled plasma mass spectrometer (MC-ICPMS) at the University of Southampton according to methods described elsewhere^{18,20,54}.

External reproducibility of $\delta^{11}\text{B}$ analyses is calculated following the approach of ref. 54, and is described by the relationship:

$$2\sigma = 1.87 \exp^{-20.6[^{11}\text{B}]} + 0.22 \exp^{-0.43[^{11}\text{B}]} \quad (1)$$

where $[^{11}\text{B}]$ is the intensity of the ^{11}B signal in volts (see ref. 18 for further details).

Trace elements were measured on a Thermo Scientific Element 2 single collector ICPMS at the University of Southampton, following established methods²⁰. Over the period 2012–2013, analytical reproducibility for Mg/Ca was $\pm 2.7\%$ (2σ). Raw Mg/Ca ratios were corrected for changes in the Mg/Ca ratio of seawater $(\text{Mg}/\text{Ca})_{\text{sw}}$, using the approach of ref. 55 and the power-law modification of ref. 56 and the modelled $(\text{Mg}/\text{Ca})_{\text{sw}}$ of ref. 57. Specifically, we use an H value⁵⁶ of 0.41, originally derived for *G. sacculifer*⁵⁸, because no species-specific H value is currently available for *G. ruber* (for extended discussion, see ref. 48). The following equation^{56,59} was therefore used to derive calcification temperatures (in units of $^{\circ}\text{C}$) from our Mg/Ca ratios, which also includes a depth correction to account for the influence of dissolution on shell Mg/Ca ratios.

$$T = \frac{\ln \left[\left(\frac{\text{Mg}}{\text{Ca}} \right)_{\text{test}} / E \left(\left(\frac{\text{Mg}}{\text{Ca}} \right)_{\text{sw}} \right)^H \right]}{0.09} + (0.61Z) \quad (2)$$

where $\left(\frac{\text{Mg}}{\text{Ca}} \right)_{\text{sw}}^t$ is the Mg/Ca ratio of seawater at the time t of interest, $\left(\frac{\text{Mg}}{\text{Ca}} \right)_{\text{test}}$ is the Mg/Ca of the foraminiferal test, Z is the core depth in kilometres and E is defined by the following equation⁵⁶:

$$E = \frac{0.38}{\left(\left(\frac{\text{Mg}}{\text{Ca}} \right)_{\text{sw}} \right)^H}$$

Trace element data were also used to check the efficiency of the foraminiferal cleaning procedure^{20,54}. All samples had Al/Ca ratios of $< 100\ \mu\text{mol mol}^{-1}$, and typically $< 60\ \mu\text{mol mol}^{-1}$.

Determination of pH from $\delta^{11}\text{B}$ of *G. ruber*. Boron in seawater exists mainly as two different species, boric acid ($\text{B}(\text{OH})_3$) and the borate ion ($\text{B}(\text{OH})_4^-$), and their relative abundance is pH dependent. There are two isotopes of boron, ^{11}B ($\sim 80\%$) and ^{10}B ($\sim 20\%$), with a ratio normally expressed in delta notation (in per mil, ‰) as:

$$\delta^{11}\text{B} = \left[\left(\frac{^{11}\text{B}/^{10}\text{B}_{\text{sample}}}{^{11}\text{B}/^{10}\text{B}_{\text{NIST951}}} \right) - 1 \right] \times 1,000 \quad (3)$$

where $^{11}\text{B}/^{10}\text{B}_{\text{NIST951}}$ is the isotopic ratio of the NIST SRM 951 boric acid standard ($^{11}\text{B}/^{10}\text{B} = 4.04367$; ref. 60).

There is a pronounced isotopic fractionation between the two dissolved boron species, with boric acid being enriched in ^{11}B by 27.2‰ (ref. 61). As the concentration of each species is pH dependent, their isotopic composition also has to change with pH in order to maintain a constant seawater $\delta^{11}\text{B}$. Calibration studies^{54,62,63} have shown that the borate species is predominantly incorporated into foraminiferal

CaCO_3 , and therefore ocean pH can be calculated from the $\delta^{11}\text{B}$ of borate ($\delta^{11}\text{B}_{\text{borate}}$) as follows:

$$\text{pH} = \text{p}K_{\text{B}}^* - \log \left(\frac{\delta^{11}\text{B}_{\text{sw}} - \delta^{11}\text{B}_{\text{borate}}}{\delta^{11}\text{B}_{\text{sw}} - (^{11,10}\text{K}_{\text{B}} \times \delta^{11}\text{B}_{\text{borate}}) - 1,000(^{11,10}\text{K}_{\text{B}} - 1)} \right) \quad (4)$$

where $\text{p}K_{\text{B}}^*$ is the dissociation constant for boric acid at *in situ* temperature, salinity and pressure⁶⁴, $\delta^{11}\text{B}_{\text{sw}}$ is the isotopic composition of seawater (39.61‰; ref. 65), $\delta^{11}\text{B}_{\text{borate}}$ is the isotopic composition of borate ion, and $^{11,10}\text{K}_{\text{B}}$ is the isotopic fractionation between the two aqueous species of boron in seawater (1.0272 ± 0.0006) (ref. 61).

In our calculations, the temperature for ODP Site 999 is derived from Mg/Ca ratios measured on aliquots (separated after dissolution) of the same samples as those used for $\delta^{11}\text{B}$ analysis and for ODP Site 662 from published records of temperature using the U_{37}^{K} proxy⁶⁶. Despite the uncertainty in Mg/Ca-derived SSTs we have not used published U_{37}^{K} temperature records for ODP Site 999 because they are of lower temporal resolution and close to saturation ($T = 28\text{--}29\ ^{\circ}\text{C}$)²⁵. Salinity has little influence on the calculations of pH ($\pm 1\ \text{psu} = \pm 0.006\ \text{pH units}$), and therefore is assumed to be constant at 35 psu (similar to the present-day mean annual average at both locations). The uncertainty associated with this assumption is propagated into $p_{\text{CO}_2}^{\text{atm}}$ calculations.

Boron has a long residence time in seawater (10–20 Myr; ref. 67), and to account for likely (small) changes in the boron isotopic composition of seawater ($\delta^{11}\text{B}_{\text{sw}}$) over the last 3 Myr, we use a simple linear extrapolation between modern $\delta^{11}\text{B}_{\text{sw}}$ (39.61‰; ref. 65) and the $\delta^{11}\text{B}_{\text{sw}}$ determined by ref. 68 for the middle Miocene (12.72 Myr ago; $\delta^{11}\text{B}_{\text{sw}} = 37.8\%$). This simple estimation yields $\delta^{11}\text{B}_{\text{sw}} = 39.2\%$ at 3 Myr ago, which is consistent with available independent constraints, for example those based on assumptions of bottom-water pH and measured benthic foraminiferal $\delta^{11}\text{B}$ (ref. 69).

Finally, to calculate pH from the $\delta^{11}\text{B}$ of *G. ruber*, it is necessary to account for species-specific differences between $\delta^{11}\text{B}_{\text{borate}}$ in ambient seawater and $\delta^{11}\text{B}$ in foraminiferal calcite ($\delta^{11}\text{B}_{\text{calcite}}$; that is, ‘vital effects’). Here we used the species- and size-specific calibration equation of ref. 18 for *G. ruber* in the size range 300–355 μm (see equation (5)). This equation has been applied in previous studies¹⁸ to produce a $\delta^{11}\text{B}$ -based $p_{\text{CO}_2}^{\text{atm}}$ record for the last 30 kyr that is in very good agreement with ice-core $p_{\text{CO}_2}^{\text{atm}}$ records (Extended Data Fig. 2).

$$\delta^{11}\text{B}_{\text{borate}} = (\delta^{11}\text{B}_{\text{calcite}} - 8.87 \pm 1.52) / 0.60 \pm 0.08 \text{ (uncertainty at } 2\sigma) \quad (5)$$

It is important to note that not only is there generally good preservation of the sites we use^{23,24}, but also the $\delta^{11}\text{B}$ of *G. ruber* does not appear to be greatly affected by partial dissolution²⁵.

Determination of $p_{\text{CO}_2}^{\text{atm}}$ from $\delta^{11}\text{B}$ -derived pH. Another variable of the ocean carbonate system is required besides pH to calculate the partial pressure of CO_2 in seawater, $p_{\text{CO}_2}^{\text{sw}}$ (ref. 70). Here, total alkalinity (TA) is assumed to be constant at values similar to modern values at ODP Site 999 ($2,330\ \mu\text{mol kg}^{-1}$; ref. 20). It is important to note that $p_{\text{CO}_2}^{\text{sw}}$ estimates are mostly determined by the reconstructed pH and that TA has little influence. This is because pH reflects the ratio of TA to DIC (total dissolved inorganic carbon), so when pH is known the ratio of TA:DIC is set, so the effect on $p_{\text{CO}_2}^{\text{sw}}$ of a large increase/decrease in TA is partially countered by an opposite change in DIC. Indeed, at a given pH, a 10% change in TA results in a $p_{\text{CO}_2}^{\text{sw}}$ change of only 10%. For example, modifying TA by $\pm 100\ \mu\text{mol kg}^{-1}$ (a range equivalent to modelled variations in TA for the last 2 Myr; ref. 30) modifies reconstructed $p_{\text{CO}_2}^{\text{sw}}$ (when pH is known) by less than $\pm 12\ \mu\text{atm}$.

$p_{\text{CO}_2}^{\text{sw}}$ was calculated using the equations of ref. 70, the ‘seacarb’ package of R (statistical software, see ref. 71) and a Monte Carlo approach ($n = 10,000$) to fully propagate the uncertainty in the input parameters (at 95% confidence or full range, where appropriate): $\delta^{11}\text{B}$ (\pm analytical uncertainty, calculated using equation (1)), and the calibration uncertainty in equation (5), the Mg/Ca-derived temperature ($\pm 3\ ^{\circ}\text{C}$), the salinity ($\pm 3\ \text{psu}$), TA ($\pm 175\ \mu\text{mol kg}^{-1}$), and $\delta^{11}\text{B}_{\text{sw}}$ ($\pm 0.4\%$). $p_{\text{CO}_2}^{\text{atm}}$ was then calculated from $p_{\text{CO}_2}^{\text{sw}}$ using Henry’s Law and subtracting the modern disequilibria with respect to CO_2 at the two sites (Extended Data Fig. 1; Supplementary Tables 1 and 2). Note that for the quoted uncertainty range for temperature, salinity, and $\delta^{11}\text{B}_{\text{sw}}$ a normal distribution is assumed. However, for TA we have assumed a ‘flat’ probability (that is, an equal probability of TA being any value in the range 2,155–2,505 $\mu\text{mol kg}^{-1}$). We therefore do not ascribe weight to the assumption that TA remains constant, but rather fully explore the likely range given the available, model-based, constraints^{72,73}. It should also be noted that salinity and temperature have little effect on our estimated $p_{\text{CO}_2}^{\text{sw}}$ ($+1\ \text{psu} = +0.2\ \mu\text{atm}$; $+1\ ^{\circ}\text{C} = +8\ \mu\text{atm}$).

Comparison with published records of Pliocene $p_{\text{CO}_2}^{\text{atm}}$. Figure 1 and Extended Data Fig. 2b, c show a comparison of our high-resolution $\delta^{11}\text{B}$ -derived $p_{\text{CO}_2}^{\text{atm}}$ record with published records. As noted in the main text, although the various approaches agree, in detail our record exhibits more structure. As a consequence, cross plots of

the previously published CO₂ data against ΔMAT (or SST_{st}) are largely incoherent (Extended Data Fig. 2d–f). In the case of the stomatal estimates⁵⁰ and the existing $\delta^{11}\text{B}$ -based records^{23,25}, this is mainly a consequence of their low temporal resolution, although analytical issues⁷⁴ and species choice (we use *G. ruber*, which spends its entire life cycle in the mixed layer, whereas ref. 23 uses *G. sacculifer*, which migrates during its life cycle and whose $\delta^{11}\text{B}$, unlike that of *G. ruber*, is modified by partial dissolution²⁵) may also have a role in the discrepancy with earlier $\delta^{11}\text{B}$ records (see ref. 25 for further discussion). The lack of variability through the Pliocene for the alkenone-based records may be related to changes in the size of the alkenone producers²⁶, fluctuations in nutrient content/water depth of maximum alkenone production, and/or variations in the degree of passive versus active uptake of CO₂ by the alkenone-producing coccolithophorids^{49,75}.

Continuous records of Plio-Pleistocene global temperature change. Robust records of global temperature change are needed to determine how Earth's climate has responded to changes in CO₂. Here we estimate this variable using two independent approaches: (1) we generate a stack of available sea surface temperature records (SST_{st}); and (2) following ref. 35 we use a reconstruction of global mean annual surface air temperature change based on a scaling of the Northern Hemisphere temperature required by a simple coupled ice-sheet–climate model to predict the benthic $\delta^{18}\text{O}$ stack of ref. 76 (tuned here to the LR04 age model; ΔMAT).

For the SST stack we imposed a number of criteria for site selection. These are: (1) the record must be continuous from the late Pliocene to the late Pleistocene (or nearly so); (2) the temporal resolution must be relatively high (ideally better than one sample per 10 kyr; for ODP Site 1237 we have, however, accepted a lower resolution to increase spatial coverage) to allow us to fully resolve the dominant orbital-scale variability; (3) the SST record must be based on U_{37}^{K} , given that Mg/Ca suffers an unacceptable level of uncertainty on these timescales owing to the secular evolution of the Mg/Ca ratio of seawater (for example, ref. 48); and (4) the temperatures recorded by the U_{37}^{K} proxy must be less than 29 °C, above which the proxy becomes saturated and therefore unresponsive⁹². Ten published records meet these criteria (ODP Sites 982, 607, 1012, 1082, 1239, 846, 662, 722, 1237 and 1090; refs 66, 77–84) and the locations of these sites are shown in Extended Data Fig. 2b. The average temporal resolution of these records is one sample about every 4 kyr (ranging from ~2 kyr to ~13 kyr) and the published age model of each site is either part of the LR04 stack or was tuned to it (see the original publications for details).

To stack the records, each was first converted to a relative SST record referenced to either the average of the Holocene (0–10 kyr), or mean annual modern SST if the Holocene is missing, and then linearly interpolated to a 5-kyr spacing. These relative records are then averaged to produce a single stacked record of relative SST change (SST_{st} ; Supplementary Table 5). The number of sites contributing to the SST stack varies but for most of the record is ≥ 8 (Extended Data Fig. 6a, b). Uncertainty on the SST stack is estimated by a Monte Carlo procedure where 1,000 realizations are made of each individual SST record with noise added reflecting the magnitude of analytical uncertainty in the U_{37}^{K} SST reconstruction (± 1 °C at 2 σ ; ref. 92). Since we are using the same proxy for each location it is not necessary to consider the calibration uncertainty, as this should be the same for each record. Each SST realization is then averaged to produce 1,000 realizations of the SST stack. The mean of these 1,000 realizations is then calculated and the 95% confidence interval is given by the 2.5% and 97.5% percentile (red band on Fig. 3). Jackknifing of the SST stack (that is, the sequential removal of one record at a time) indicates that no particular record has undue influence and the SST stack remains close to the bounds relating to analytical uncertainty (the grey lines on Extended Data Fig. 6c, d).

Our aim with the SST stack was not specifically to reconstruct global SST change but rather to examine the change in SST at these locations for a given forcing in the Pliocene and Pleistocene. We therefore do not require the SST stack to reflect global SST change. However, in order to assess how well the SST stack does reflect global SST we: (1) Examined the mean of historic SST change (1870 AD to 2013 AD; from the HadISST database; ref. 85) at each location where we have an alkenone palaeo-SST record. This comparison is shown in Extended Data Fig. 7 (blue circles). Despite exhibiting more variability than the mean annual global average (red in Extended Data Fig. 7), these ten sites clearly capture the global long-term trend in global mean $\text{SST}^{86,87}$ over the last 140 years or so (Extended Data Fig. 7). (2) Compared the SST stack to a multi-proxy and more comprehensive and independent compilation of ref. 32 that covers the last 100 kyr with >30 sites and the last 278 kyr with >10 sites. When data for the last 278 kyr are stacked together in a similar way to the SST stack, the stack of ref. 32 (blue on Fig. 3c) compares well with SST_{st} , giving us confidence that it closely reflects global SST change. (3) Compared the SST stack to discrete global reconstructions of SST. For the last glacial (20–25 kyr), the SST stack gives a ΔSST of -2.2 ± 0.4 K, which is close to the ΔSST of -3.2 K from a recent comprehensive compilation for the Last Glacial Maximum⁴¹ and is within uncertainty of earlier reconstructions (for example, ref. 91 where ΔSST of -1.9 ± 1.8 K). For the Mid-Pliocene Warm Period (3–3.3 Myr ago), our SST stack gives an average of $+2.3$ K. A simple mean calculated from the larger multi-proxy

PRISM SST compilation of ref. 40 is very similar at $+2.6$ K. The SST stack is slightly warmer than an area-weighted mean of the PRISM SST set ($+2$ K; ref. 40).

Taken together, these comparisons clearly indicate that, although SST_{st} is made of a limited number of sites, it does appear to closely reflect change in global SST. This conclusion is also supported by the general agreement between the trends (but not absolute values) exhibited by ΔMAT and the SST stack through the Pliocene and Pleistocene (Fig. 3), with subtle differences between these two climate records (for example, at 2.8 Myr ago) potentially a result of a decoupling between deep- and surface-water temperature evolution, small spatial biases in our SST stack, and/or minor age-model inaccuracies (the conversion of depth below seafloor in a marine sediment core to age).

Regression-based determinations of climate sensitivity. To examine the climatic response (expressed as either ΔMAT or ΔSST) to forcing by CO₂ and land-ice albedo changes in both time periods, we used a linear regression approach. Because each variable used (CO₂ and sea level, ΔMAT or ΔSST) has an associated uncertainty, however, it is necessary to fully explore the influence of these uncertainties on our estimates of slope determined using least-squares linear regression. Owing to the difficulty of performing the least-squares linear regression with uncertainty in x and y variables that are not necessarily normally distributed, we have used a two-stage approach to fully propagate all the uncertainties involved. First, we generated 1,000 realizations of each temporal record of each variable (for example, ΔF_{CO_2} , $\Delta F_{\text{CO}_2,\text{L}}$, ΔMAT or ΔSST) based on a random sampling of each record within its uncertainty envelope. This uncertainty envelope was either a simple normal distribution (for example, ± 6 parts per million for ice-core CO₂) or based on other Monte Carlo output (for example, random sampling of the 10,000 simulations of the Pliocene $\delta^{11}\text{B}$ - $p_{\text{CO}_2}^{\text{atm}}$ record or the 1,000 realizations of the SST stack; see above). Then the first realization of the ΔF_{CO_2} (or $\Delta F_{\text{CO}_2,\text{L}}$) record was regressed against the first realization of the ΔMAT (or ΔSST) with the uncertainty in the slope and intercept of that regression determined using a bootstrapping approach ($n = 1,000$; ref. 88). The second realization of the forcing term and the climate response was then regressed and the 1,000 estimates of slope and intercept by bootstrapping were combined with 1,000 of the first regression. This continued for all 1,000 realizations and a probability density function for the slope and intercept, accounting for x and y uncertainty, was then constructed from the combined bootstrap estimates for each realization ($n = 1,000,000$). The results of this approach are shown in Fig. 5.

As noted above, $p_{\text{CO}_2}^{\text{atm}}$ (and hence ΔF_{CO_2}) calculated from boron isotopes is a function of not only the measured $\delta^{11}\text{B}$ but also the total alkalinity (TA; or other second carbonate system variable) and, beyond the last million years or so, the boron isotopic composition of seawater ($\delta^{11}\text{B}_{\text{sw}}$). This is illustrated in Extended Data Fig. 8. Here $p_{\text{CO}_2}^{\text{atm}}$ is calculated from an artificial $\delta^{11}\text{B}$ and temperature record (Extended Data Fig. 8a), a TA of either 2,000 $\mu\text{mol kg}^{-1}$, 2,300 $\mu\text{mol kg}^{-1}$ or 2,600 $\mu\text{mol kg}^{-1}$, a $\delta^{11}\text{B}_{\text{sw}}$ of 38.8‰, 39.6‰ (that is, modern) or 40.4‰ (Extended Data Fig. 8) and the assumption that $p_{\text{CO}_2}^{\text{atm}} = p_{\text{CO}_2}^{\text{sw}}$. These parameter choices result in a large difference in absolute CO₂ but, although they are extreme and perhaps unlikely for the Pliocene, the slope of a linear regression of global temperature change and ΔF_{CO_2} is very similar for each set of parameters (Extended Data Fig. 8c, d). So much so, that even with only a poor knowledge of $\delta^{11}\text{B}_{\text{sw}}$ (for example, ± 0.8 ‰) and TA (for example, ± 300 $\mu\text{mol kg}^{-1}$) the accuracy of the relationship between reconstructed ΔF_{CO_2} and temperature is not unduly affected.

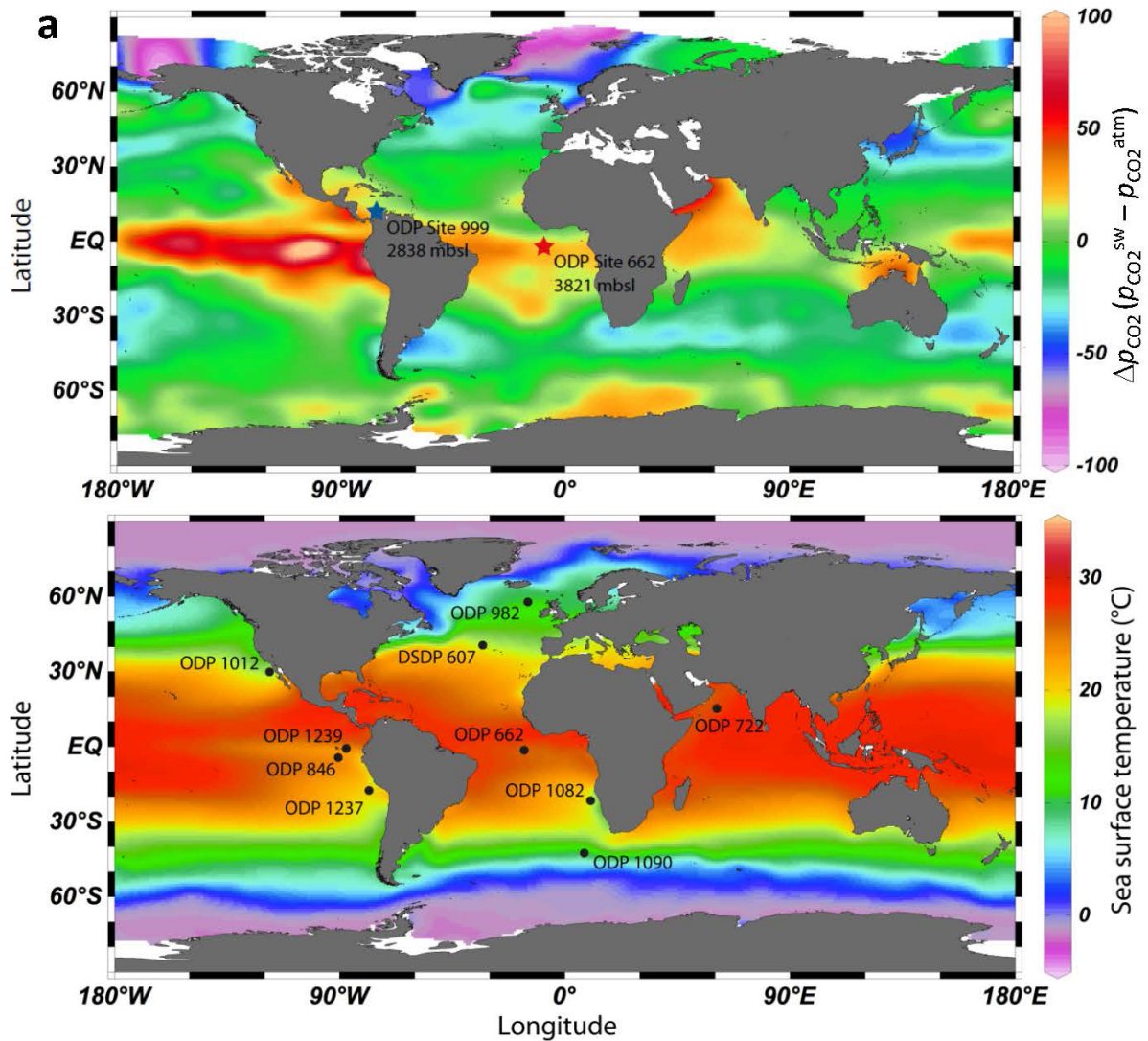
The residence time of boron in seawater (10–20 Myr) ensures that changes in $\delta^{11}\text{B}_{\text{sw}}$ across the time interval examined here (1 Myr) are unlikely to be large (<0.1‰; ref. 67) and so uncertainty in the absolute value of $\delta^{11}\text{B}_{\text{sw}}$ and any changes across the study interval can be ignored for our determinations of S^{P} . In all the previous calculations we assume that TA is randomly distributed between 2,155 $\mu\text{mol kg}^{-1}$ and 2,505 $\mu\text{mol kg}^{-1}$, therefore accounting for all possible trends in TA across the time interval studied within this range. However, to better examine the influence of a large secular shift in TA on our estimates of S^{P} we have imposed a 200 $\mu\text{mol kg}^{-1}$ decrease (TA_d) or increase (TA_i) across our Pliocene study interval. The slope for the regressions using one parameter set (VDW11 and sea level values from ref. 46 recalculated by ref. 12) but with such a varying TA are shown in Extended Data Fig. 8e, f. Even this relatively large secular change does not have a major influence on the estimated slope, clearly illustrating that our assumptions regarding TA, both its absolute value and its secular evolution, have little influence on our calculated ΔF_{CO_2} and hence our conclusions.

Pliocene $p_{\text{CO}_2}^{\text{atm}}$ variability. The apparent cyclicity in our Pliocene CO₂ record can be investigated using spectral analysis. Extended Data Fig. 4c shows that the evolutive power spectra for the Pliocene $p_{\text{CO}_2}^{\text{atm}}$ and a ~100-kyr cycle is clearly dominant. Our sampling resolution is one sample per ~13 kyr, which is not sufficient to resolve cycles of a precessional length (for example, 19 kyr and 23 kyr) but may be adequate to resolve obliquity (~41-kyr length), yet these cycles are apparently absent in the generated spectra (Extended Data Fig. 4c). To ensure our resolution is not biasing this result we have sampled the LR04 benthic $\delta^{18}\text{O}$ stack at our exact sampling resolution and examined the evolutive power spectra of this

sampled record (Extended Data Fig. 4d). This analysis reveals the presence of 100-kyr and 41-kyr cycles in the $\delta^{18}\text{O}$ data, despite our relatively low resolution, supporting the observation that the dominant cycle in Pliocene $p\text{CO}_2^{\text{atm}}$ is ~ 100 kyr.

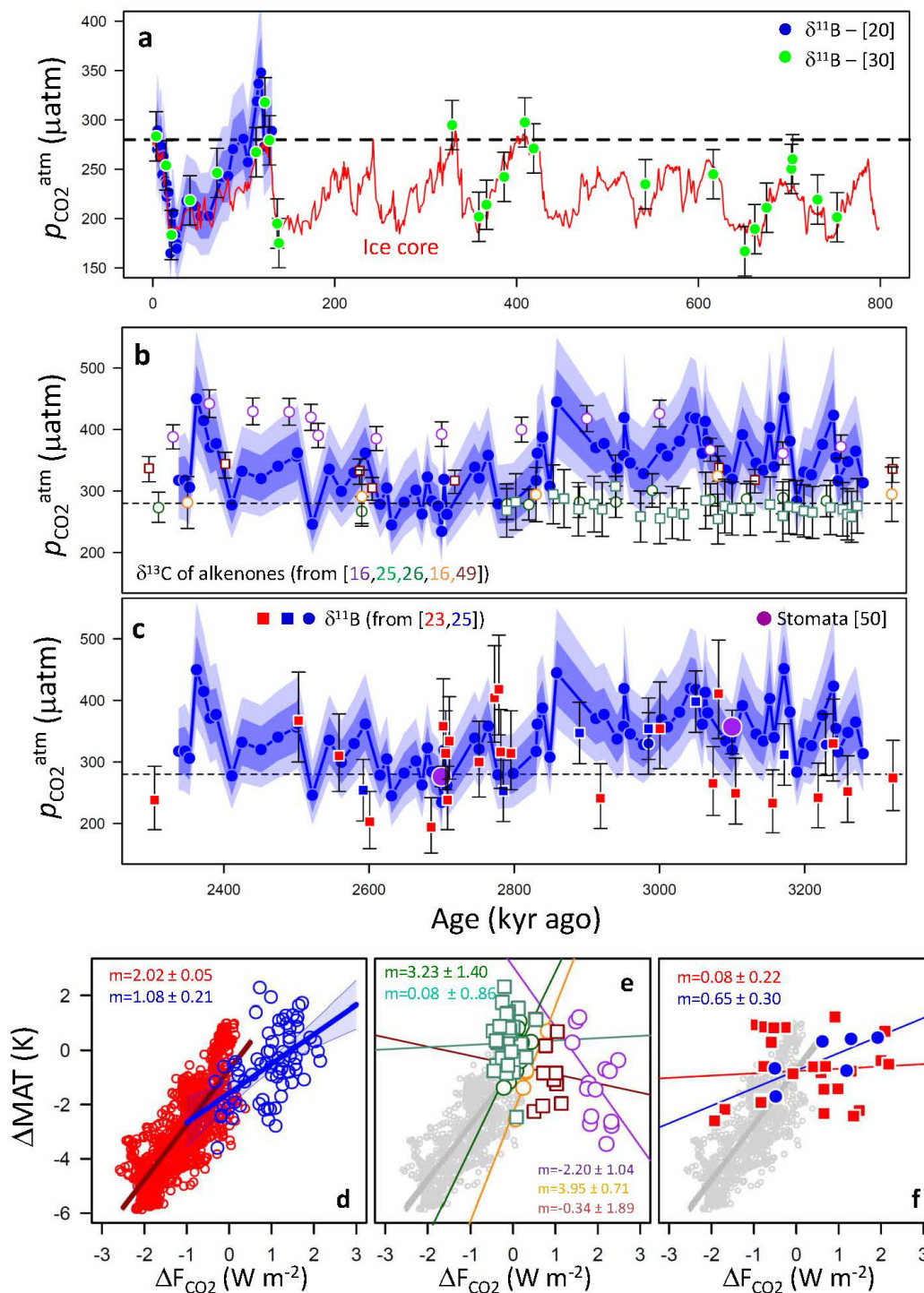
The magnitude of Pliocene $p\text{CO}_2^{\text{atm}}$ variability, shown in Extended Data Fig. 4a, is similar to that exhibited by published late and mid-Pleistocene $\delta^{11}\text{B}-p\text{CO}_2^{\text{atm}}$ records (green and red lines on Extended Data Fig. 4a) and by the Late Pleistocene ice-core data when noise that is approximately equivalent to our $\delta^{11}\text{B}-p\text{CO}_2^{\text{atm}}$ uncertainty is added (± 35 μatm ; black dashed line on Extended Data Fig. 4a). In contrast, the $\delta^{18}\text{O}$ variability for these time intervals increases markedly from the Pliocene to late Pleistocene as the magnitude of glacial–interglacial cycles increases (Fig. 1e, Extended Data Fig. 4b).

51. Lawrence, K. T. *et al.* Time-transgressive productivity changes in the North Atlantic upon Northern Hemisphere glaciation. *Paleoceanography* **28**, 740–751 (2013).
52. Barker, S., Greaves, M. & Elderfield, H. A study of cleaning procedures used for foraminiferal Mg/Ca paleothermometry. *Geochem. Geophys. Geosyst.* **4**, 8407 (2003).
53. Yu, J., Elderfield, H., Greaves, M. & Day, J. Preferential dissolution of benthic foraminiferal calcite during laboratory reductive cleaning. *Geochem. Geophys. Geosyst.* **8**, Q06016 (2007).
54. Rae, J. W. B., Foster, G. L., Schmidt, D. N. & Elliott, T. Boron isotopes and B/Ca in benthic foraminifera: proxies for the deep ocean carbonate system. *Earth Planet. Sci. Lett.* **302**, 403–413 (2011).
55. Medina-Elizalde, M., Lea, D. W. & Fantle, M. S. Implications of seawater Mg/Ca variability for Plio-Pleistocene tropical climate reconstruction. *Earth Planet. Sci. Lett.* **269**, 585–595 (2008).
56. Evans, D. & Muller, W. Deep time foraminifera Mg/Ca paleothermometry: nonlinear correction for secular change in seawater Mg/Ca. *Paleoceanography* **27**, PA4205 (2012).
57. Fantle, M. S. & DePaolo, D. J. Sr isotopes and pore fluid chemistry in carbonate sediment of the Ontong Java Plateau: calcite recrystallisation rates and evidence for a rapid rise in seawater Mg over the last 10 million years. *Geochim. Cosmochim. Acta* **70**, 3883–3904 (2006).
58. Delaney, M. L., Bé, W. H. A. & Boyle, E. A. Li, Sr, Mg, and Na in foraminiferal calcite shells from laboratory culture, sediment traps, and sediment cores. *Geochim. Cosmochim. Acta* **49**, 1327–1341 (1985).
59. Dekens, P. S., Lea, D. W., Pak, D. K. & Spero, H. J. Core top calibration of Mg/Ca in tropical foraminifera: refining paleotemperature estimation. *Geochem. Geophys. Geosyst.* **3**, <http://dx.doi.org/10.1029/2001GC000200> (2002).
60. Catanzaro, E. J. *et al.* *Boric Assay; Isotopic, and Assay Standard Reference Materials* (US National Bureau of Standards Special Publication 260-17, 1970).
61. Klochko, K., Kaufman, A. J., Yoa, W., Byrne, R. H. & Tossell, J. A. Experimental measurement of boron isotope fractionation in seawater. *Earth Planet. Sci. Lett.* **248**, 276–285 (2006).
62. Hemming, N. G. & Hanson, G. N. Boron isotopic composition and concentration in modern marine carbonates. *Geochim. Cosmochim. Acta* **56**, 537–543 (1992).
63. Hemming, N. G., Reeder, R. J. & Hanson, G. N. Mineral-fluid partitioning and isotopic fractionation of boron in synthetic calcium carbonate. *Geochim. Cosmochim. Acta* **59**, 371–379 (1995).
64. Dickson, A. G. Thermodynamics of the dissociation of boric-acid in synthetic seawater from 273.15 to 318.15 K. *Deep-Sea Res.* **37**, 755–766 (1990).
65. Foster, G. L., Pogge von Strandmann, P. A. E. & Rae, J. W. B. Boron and magnesium isotopic composition of seawater. *Geochem. Geophys. Geosyst.* **11**, Q08015 (2010).
66. Herbert, T. D., Cleaveland Peterson, L., Lawrence, K. T. & Liu, Z. Tropical ocean temperatures over the past 3.5 million years. *Science* **328**, 1530–1534 (2010).
67. Lemarchand, D., Gaillardet, J., Lewin, E. & Allegre, C. J. Boron isotope systematics in large rivers: implications for the marine boron budget and paleo-pH reconstruction over the Cenozoic. *Chem. Geol.* **190**, 123–140 (2002).
68. Foster, G. L., Lear, C. H. & Rae, J. W. B. The evolution of $p\text{CO}_2$, ice volume and climate during the middle Miocene. *Earth Planet. Sci. Lett.* **341–344**, 243–254 (2012).
69. Raitzsch, H. B. Cenozoic boron isotope variations in benthic foraminifers. *Geology* **41**, 591–594 (2013).
70. Zeebe, R. & Wolf-Gladrow, D. A. *CO₂ in Seawater: Equilibrium, Kinetics, Isotopes* (Elsevier Oceanography Series 65, 2001).
71. R Core Team. *R: a Language and Environment for Statistical Computing* <http://www.R-project.org/> (R Foundation for Statistical Computing, 2013).
72. Tyrrell, T. & Zeebe, R. E. History of carbonate ion concentration over the last 100 million years. *Geochim. Cosmochim. Acta* **68**, 3521–3530 (2004).
73. Clark, P. U. *et al.* The middle Pleistocene transition: characteristics, mechanisms, and implications for long-term changes in $p\text{CO}_2$. *Quat. Sci. Rev.* **25**, 3150–3184 (2006).
74. Foster, G. L. *et al.* Interlaboratory comparison of boron isotope analyses of boric acid, seawater and marine CaCO_3 by MC-ICPMS and NTIMS. *Chem. Geol.* **358**, 1–14 (2013).
75. Bolton, C. T. & Stoll, H. M. Late Miocene threshold response of marine algae to carbon dioxide limitation. *Nature* **500**, 558–562 (2013).
76. Zachos, J., Pagani, M., Sloan, L., Thomas, E. & Billups, K. Trends, rhythms, and aberrations in global climate 65 Ma to present. *Science* **292**, 686–693 (2001).
77. Lawrence, K. T., Herbert, T. D., Brown, C. M., Raymo, M. E. & Haywood, A. M. High-amplitude variations in North Atlantic sea surface temperature during the early Pliocene warm period. *Paleoceanography* **24**, PA2218 (2009).
78. Lawrence, K. T., Sosdian, S., White, J. M. & Rosenthal, Y. North Atlantic climate evolution through the Plio-Pleistocene climate transitions. *Earth Planet. Sci. Lett.* **300**, 329–342 (2010).
79. Brierley, C. M. *et al.* Greatly expanded tropical warm pool and weakened Hadley Circulation in the Early Pliocene. *Science* **323**, 1714–1718 (2009).
80. Etourneau, J., Martinez, P., Blanz, T. & Schneider, R. Pliocene-Pleistocene variability of upwelling activity, productivity, and nutrient cycling in the Benguela region. *Geology* **37**, 871–874 (2009).
81. Etourneau, J., Schneider, R., Blanz, T. & Martinez, P. Intensification of the Walker and Hadley atmospheric circulations during the Pliocene-Pleistocene climate transition. *Earth Planet. Sci. Lett.* **297**, 103–110 (2010).
82. Lawrence, K. T., Liu, Z. & Herbert, T. D. Evolution of the eastern tropical Pacific through Plio-Pleistocene glaciation. *Science* **312**, 79–83 (2006).
83. Martinez-Garcia, A., Rosell-Melé, A., McClymont, E. L., Gersonde, R. & Haug, G. H. Subpolar link to the emergence of the modern equatorial Pacific cold tongue. *Science* **328**, 1550–1553 (2010).
84. Dekens, P. S., Ravelo, A. C. & McCarthy, M. D. Warm upwelling regions in the Pliocene warm period. *Paleoceanography* **22**, PA3211 22 (2007).
85. Rayner, N. A. *et al.* Global analyses of sea surface temperature, sea ice, and night marine air temperature since the late nineteenth century. *J. Geophys. Res.* **D 108**, 4407 (2003).
86. Kennedy, J. J., Rayner, N. A., Smith, R. O., Parker, D. E. & Saunby, M. Reassessing biases and other uncertainties in sea surface temperature observations in situ since 1850: 1. Measurement and sampling uncertainty. *J. Geophys. Res.* **116**, D14103 (2011a).
87. Kennedy, J. J., Rayner, N. A., Smith, R. O., Parker, D. E. & Saunby, M. Reassessing biases and other uncertainties in sea surface temperature observations measured in situ since 1850: 2. Biases and homogenization. *J. Geophys. Res.* **116**, D14104 (2011b).
88. Efron, B. Bootstrap methods: another look at the jackknife. *Ann. Stat.* **7**, 1–26 (1979).
89. Locarnini, R. A. *et al.* *World Ocean Atlas 2013, Volume 1: Temperature* (NOAA Atlas NESDIS 73, 2013).
90. Schlitzer, R. *Ocean Data View* <http://odv.awi.de> (2012).
91. Waelbroeck, C. *et al.* Constraints on the magnitude and patterns of ocean cooling at the Last Glacial Maximum. *Nature Geosci.* **2**, 127–132 (2009).
92. Müller, P. J., Kirst, G., Ruhland, G., Von Storch, I. & Rosell-Melé, A. Calibration of the alkenone paleotemperature index UK'37 based on core-tops from the eastern South Atlantic and the global ocean (60 N–60 S). *Geochim. Cosmochim. Acta* **62**, 1757–1772 (1998).
93. Siddall, M. *et al.* Sea-level fluctuations during the last glacial cycle. *Nature* **423**, 853–858 (2003).



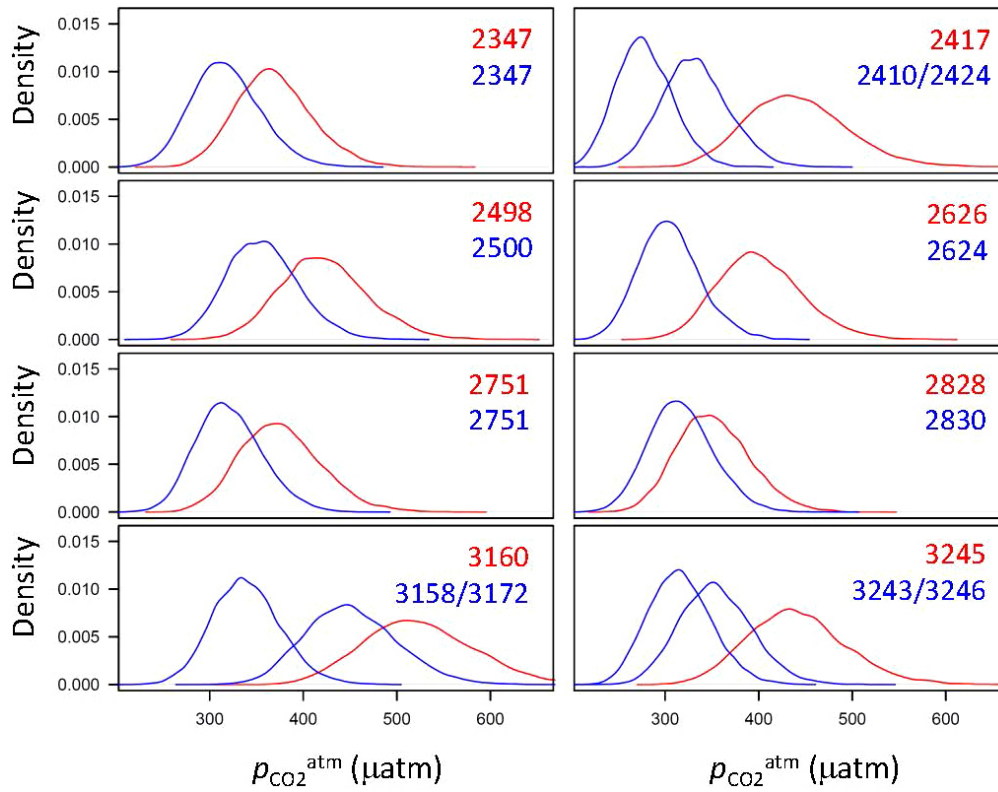
Extended Data Figure 1 | Maps of modern mean annual Δp_{CO_2} and SST labelled with site locations. a, Map of sites used for $p_{\text{CO}_2}^{\text{atm}}$ reconstructions with the mean annual modern Δp_{CO_2} from the reconstruction of ref. 21. b, Map of the sites (and labelled with their depths) used to generate the SST stack with

mean annual modern SST from the World Ocean Atlas 2013 (ref. 89). mbsl, metres below sea level, where DSDP is the Deep Sea Drilling Project. Figures constructed and data visualized in Ocean Data View⁹⁰.



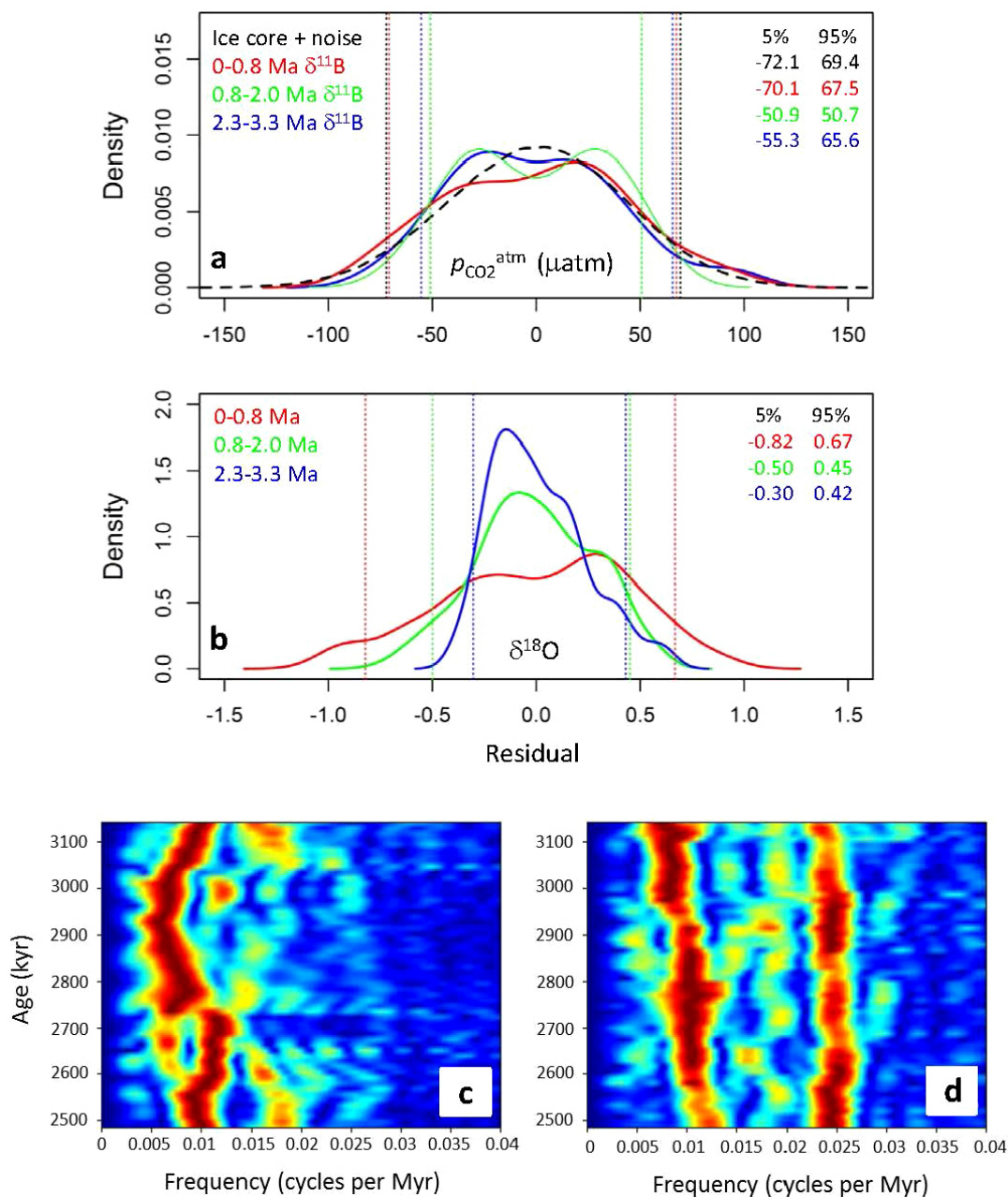
Extended Data Figure 2 | Comparisons of boron-isotope-based $p_{\text{CO}_2}^{\text{atm}}$ estimates with other methodologies and archives. **a**, Estimates of $p_{\text{CO}_2}^{\text{atm}}$ from published $\delta^{11}\text{B}$ records compared to ice-core CO_2 (red line; refs 27–29). The dotted line is for $p_{\text{CO}_2} = 278 \mu\text{atm}$. In **a** the data of ref. 20 (blue circles) have been recalculated in the same manner as described here for the Pliocene, including using the *G. ruber* $\delta^{11}\text{B}$ -pH calibration of ref. 18. The error band encompasses 68% (dark blue) and 95% (light blue) of 10,000 Monte Carlo simulations of $p_{\text{CO}_2}^{\text{atm}}$ (see main text). Also shown are the *G. sacculifer*-based $\delta^{11}\text{B}$ - $p_{\text{CO}_2}^{\text{atm}}$ record of ref. 30 (green circles). In this case error bars ($\pm 25 \mu\text{atm}$) are as determined in that study. Despite similar analytical uncertainty, the smaller error bars for the ref. 30 data result from these authors not propagating the $\delta^{11}\text{B}$ -pH calibration uncertainty and considering a smaller range in temperature, salinity and alkalinity uncertainty than in this study ($\pm 0.76^\circ\text{C}$, $\pm 1 \text{ psu}$, $\pm 27 \mu\text{mol kg}^{-1}$ versus $\pm 3^\circ\text{C}$, ± 3 practical salinity units (psu), $\pm 175 \mu\text{mol kg}^{-1}$ with a flat probability in this study). **b**, $\delta^{11}\text{B}$ -based $p_{\text{CO}_2}^{\text{atm}}$

record generated here (blue closed circles and 95% and 68% uncertainty bands) with $p_{\text{CO}_2}^{\text{atm}}$ from the $\delta^{13}\text{C}$ of alkenones from published studies. See Fig. 1 legend for details. **c**, $\delta^{11}\text{B}$ -based $p_{\text{CO}_2}^{\text{atm}}$ record generated here (blue closed circles and 95% and 68% uncertainty bands) with $p_{\text{CO}_2}^{\text{atm}}$ from previous $\delta^{11}\text{B}$ -based studies and from plant stomata. See Fig. 1 legend for details. **d–f**, Comparison of cross plots of CO_2 forcing and ΔMAT for our high-resolution $\delta^{11}\text{B}$ - CO_2 record (**d**), published alkenone CO_2 data (**e**) and published low-resolution $\delta^{11}\text{B}$ - CO_2 data (**f**). In each panel the slopes of regression lines fitted through the data are labelled (± 1 standard error, se). In **d** ice-core CO_2 data are shown as red open circles and Pliocene $\delta^{11}\text{B}$ - CO_2 as open blue circles. In **e** and **f**, ice-core CO_2 data are shown in grey for clarity. In **e**, alkenone CO_2 data are from the following sources: ODP 1208 (orange¹⁶), ODP 806 (purple¹⁶); ODP 925 (brown⁴⁹); ODP 999 (green circles²⁵; green squares²⁶). In **c** $\delta^{11}\text{B}$ - CO_2 data are from ODP 999 (blue²⁵ and red²³).



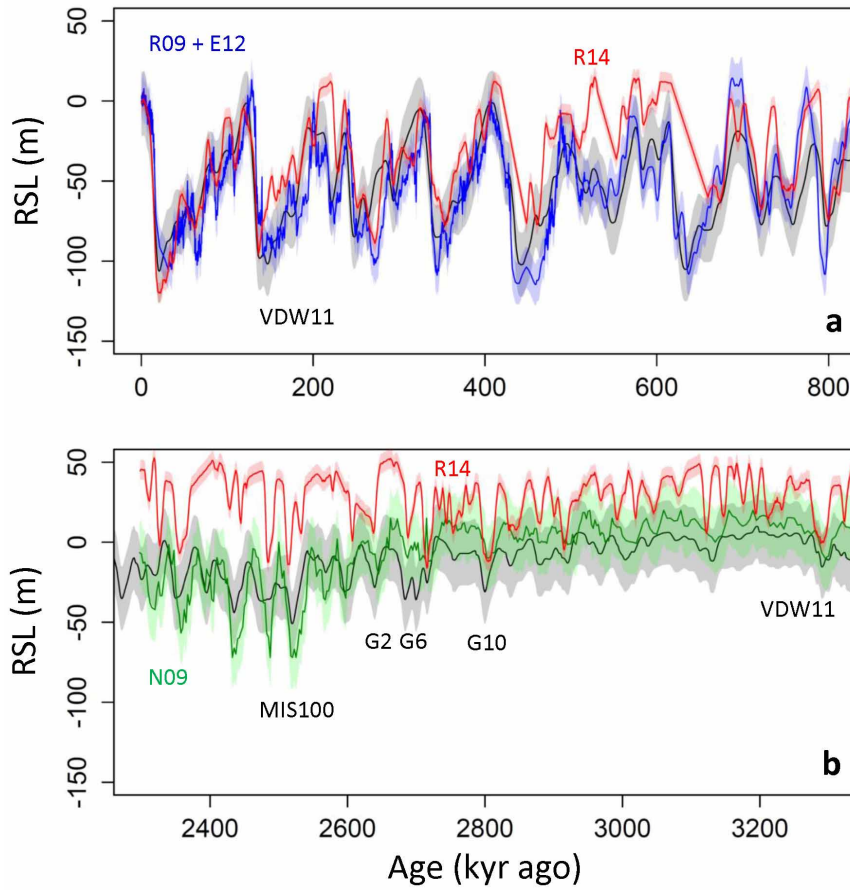
Extended Data Figure 3 | Probability density functions for equivalently aged samples from ODP Site 662 and ODP Site 999. Each panel, labelled with age (in units of kyr ago), shows the probability density function for a given estimate of $p_{\text{CO}_2}^{\text{atm}}$ from ODP Site 662 (red) and ODP Site 999 (blue). In most instances equal age samples are compared, but in some cases either where

variability is high and/or equivalent age samples are absent, we show neighbouring samples from ODP Site 999 (for example, bottom left and right). This comparison indicates that although the mean $p_{\text{CO}_2}^{\text{atm}}$ of ODP 662 tends to be higher than ODP 999, there is always a high degree of overlap between the estimates from the two sites.



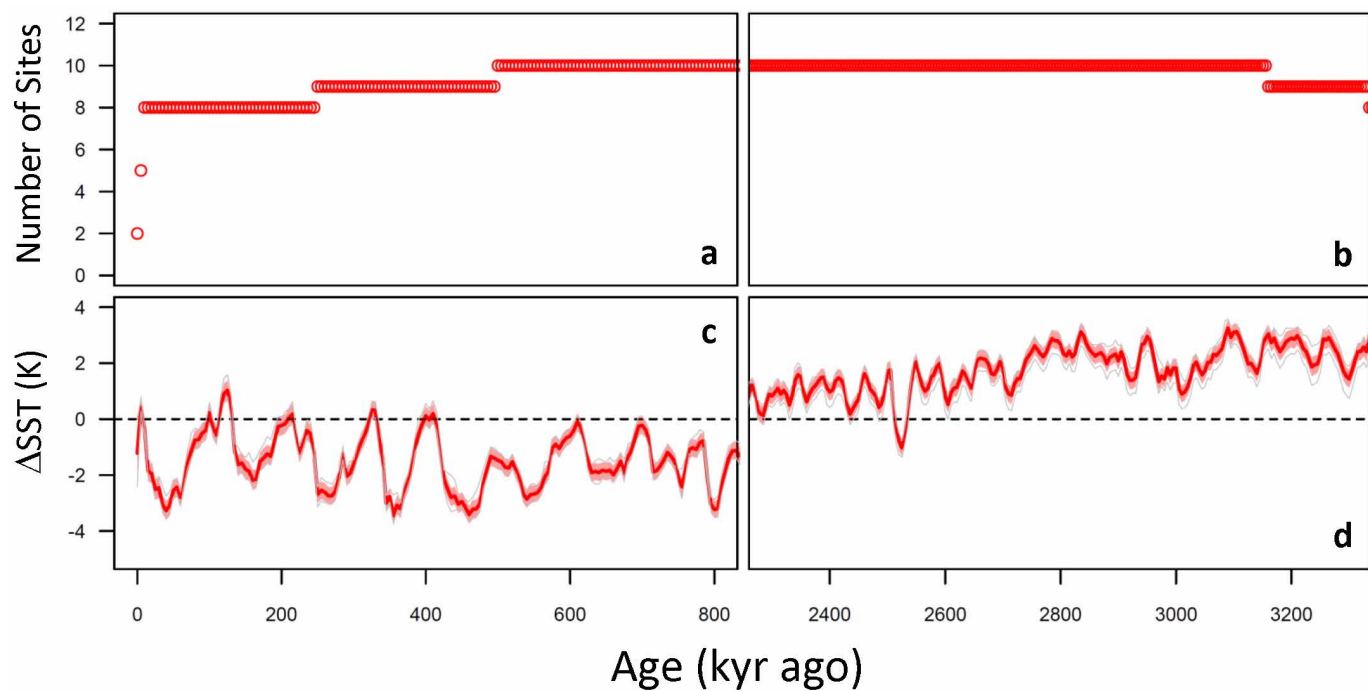
Extended Data Figure 4 | Probability density functions of $p_{\text{CO}_2}^{\text{atm}}$ and benthic $\delta^{18}\text{O}$ and time series analysis. **a**, Probability density functions of the residuals of $\delta^{11}\text{B}-p_{\text{CO}_2}^{\text{atm}}$ about the long-term trend for the late Pliocene (this study; blue line), the mid-Pleistocene³⁰ (green line) and late Pleistocene^{19,20} (red line). Dashed vertical lines show the upper and lower limit (labelled) encompassing 90% of the data. The residual of the ice-core CO_2 record²⁷⁻²⁹ about the long-term mean for 0-0.8 Myr ago plus a random noise equivalent to $\pm 35 \mu\text{atm}$ (the typical $\delta^{11}\text{B}-\text{CO}_2$ uncertainty) is shown as a black dashed probability density function. **b**, Probability density functions of the residual of LR04 benthic $\delta^{18}\text{O}$ from the long-term trend for the late Pleistocene (red),

mid-Pleistocene (green) and late Pliocene (blue). Dashed vertical lines show the upper and lower limit (labelled) encompassing 90% of the data. In contrast to $p_{\text{CO}_2}^{\text{atm}}$, $\delta^{18}\text{O}$ clearly exhibits an increase in variability over the last 3.3 Myr. **c**, **d**, Evolutionary power spectral analyses of Pliocene $p_{\text{CO}_2}^{\text{atm}}$ (**c**) and resampled $\delta^{18}\text{O}$ (ref. 22) (**d**). The evolutionary power spectra was computed using the fast Fourier transform of overlapping segments with a 300-kyr moving window. Before spectral analysis, all series were notch-filtered to remove the long-term trend (bandwidth = 0.005), and interpolated to 12-kyr intervals (the real resolution of our record is ~ 13.5 kyr).



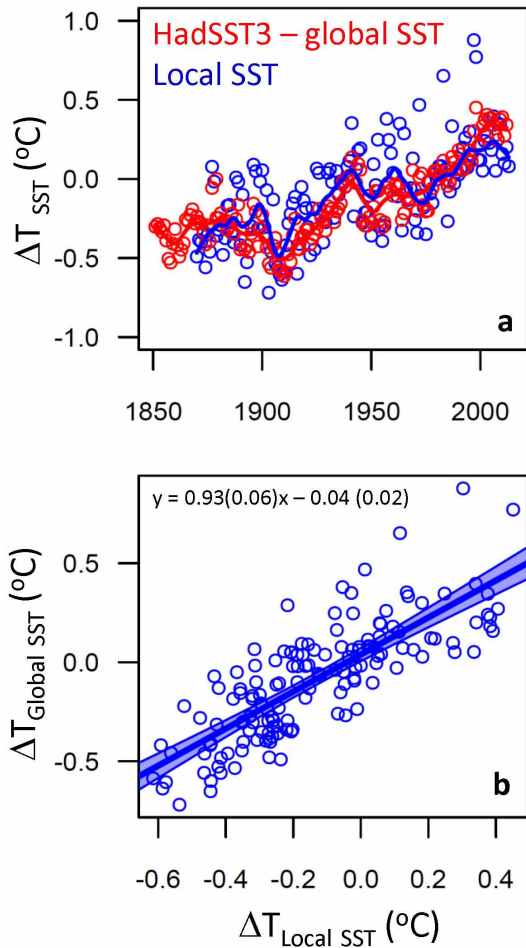
Extended Data Figure 5 | Summary of sea-level records used to calculate ΔF_{LI} . In **a** and **b** the red curve is from ref. 13 (R14) based on the planktic $\delta^{18}O$ from the Mediterranean Sea and the methods developed for the Red Sea by ref. 93. We have removed those intervals identified as possible sapropel (organic-matter-rich sediments) events and linearly interpolated across gaps in the original record. The black curve is the sea-level record from an inversion of the benthic oxygen isotope record of ref. 76 (tuned to LR04 here) using an ice sheet model³⁵ (VDW11). The blue curve in **a** is based on the planktic/bulk

$\delta^{18}O$ from the Red Sea⁴⁴ for the interval 0–520 kyr and the paired Mg/Ca and benthic $\delta^{18}O$ from the deep South Pacific for the interval 520–800 kyr (ref. 45) (R09 + E12). The green curve in **b** is based on a scaling of the LR04 $\delta^{18}O$ stack to indicators of sea level from sequence stratigraphy (ref. 46 recalculated by ref. 12). In each the uncertainty in the reconstruction at 95% confidence is shown by an appropriately coloured error band. Marine isotope stages mentioned in text are labelled. RSL, relative sea-level change (in metres), relative to the modern value.

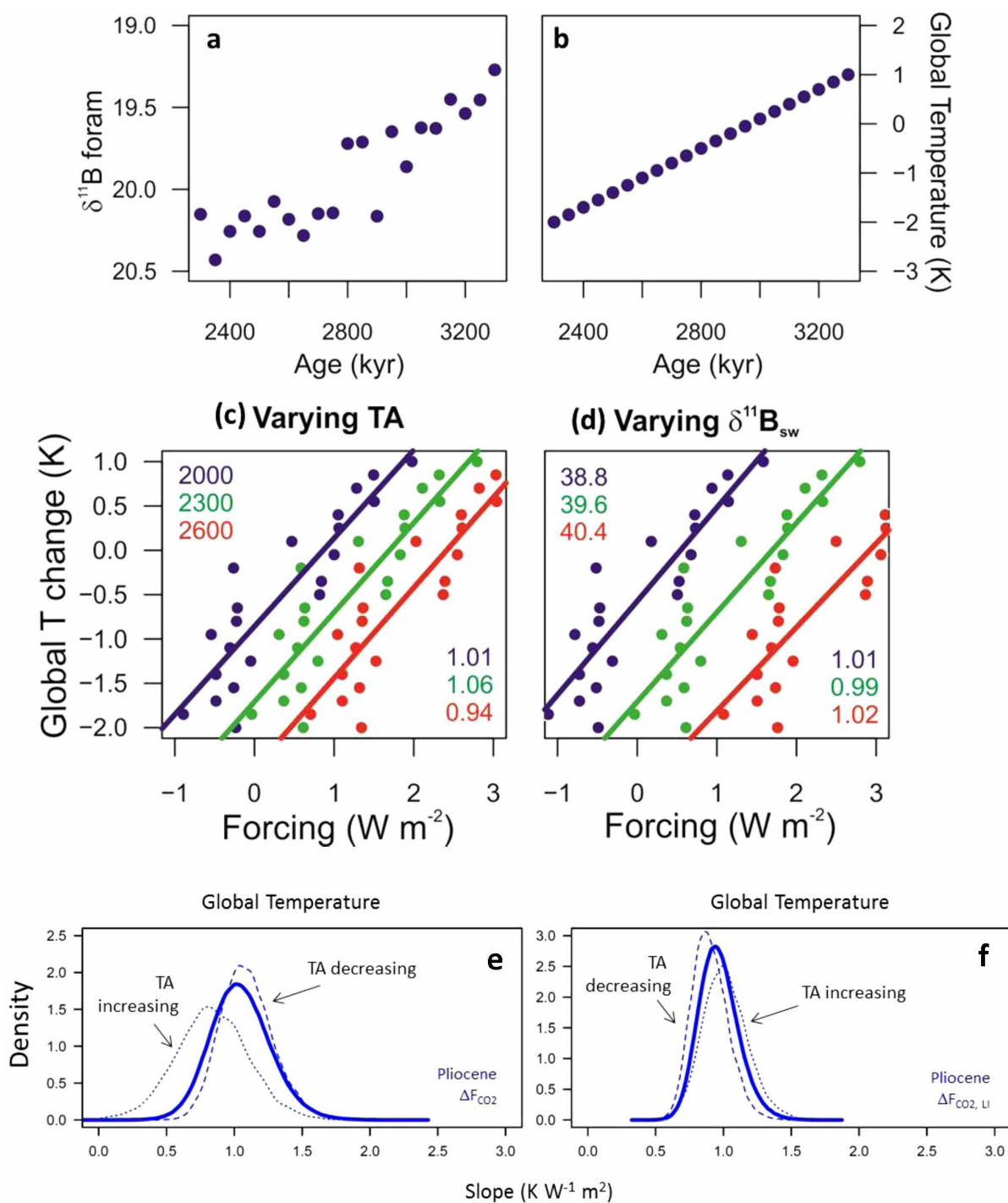


Extended Data Figure 6 | Stacked sea surface temperature record.
a, b, Number of records that contribute to the SST stack through time.
c, d, Uncertainty in the SST stack due to analytical uncertainty (at 95% confidence; red band) and showing the influence of jackknifing (that is,

removing one record at a time; grey lines show maximum and minimum). Note that the jackknifing illustrates that no single record has an undue influence on the SST stack.



Extended Data Figure 7 | Comparison of global SST from the HadSST3 data set with SST HadISST1 from ODP sites. **a**, Historic global mean annual sea surface temperature anomaly from the HadSST3 data set^{86,87} (red circles) and mean SST at locations above the ODP sites that make up the SST stack from HadISST1 (blue; local SST). Thick red and blue lines are non-parametric smoothers through both data sets. **b**, Cross plot of global mean annual SST and local SST. The regression line determined using linear regression has a slope of ~ 1 and intercept of close to 0, so local SST captures the global trend well. The shaded blue band in **b** represents the 95% confidence interval of the regression line.



Extended Data Figure 8 | The influence of TA and $\delta^{11}\text{B}_{\text{sw}}$ on determinations of S^{P} using linear regression. **a, b**, Artificial $\delta^{11}\text{B}$ record (where $\delta^{11}\text{B}$ foram is the boron isotopic composition of an artificial foraminifera; **a**) and temperature record (**b**). **c, d**, Cross plot and regressions of $\delta^{11}\text{B}-\Delta F_{\text{CO}_2}$ and global temperature for TA dramatically varying in the range 2,000–2,600 $\mu\text{mol kg}^{-1}$ (TA; **c**) and $\delta^{11}\text{B}_{\text{sw}}$ from 38.8‰ to 40.4‰ (**d**). The slopes of

the regressions, which are very similar regardless of parameter choice, are colour-coded and listed in the bottom right-hand corner of **c** and **d**. **e, f**, Probability density function of slope for regressions of Pliocene-aged ΔMAT against ΔF_{CO_2} (**e**) and $\Delta F_{\text{CO}_2, \text{LI}}$ (**f**), where TA is decreasing by 200 $\mu\text{mol kg}^{-1}$ (dashed) and increasing by 200 $\mu\text{mol kg}^{-1}$ (dotted). Note that despite large variations in TA the slope of the regressions do not change greatly.